Electron Transport in Multiwall Carbon Nanotubes

INAUGURALDISSERTATION

zur
Erlangung der Würde eines Doktors der Philosophie
vorgelegt der
Philosophisch-Naturwissenschaftlichen Fakultät
der Universität Basel
von

Mark Robertus Buitelaar

aus Den Haag (NL)

Basel, 2004

Genehmigt von der Philosophisch-Naturwissenschaftlichen Fakultät auf Antrag der Herren Professoren:

Prof. Dr. C. Schönenberger
Dr. A. Bachtold
Prof. Dr. H. Grabert
Prof. Dr. L. Kouwenhoven

Basel, den 4. Juni 2002

Prof. Dr. A. Zuberbühler, Dekan

Contents

Chapter 1

Introduction

When in 1991 the Japanese scientist Sumio Iijima studied the carbon soot created by a direct current arc-discharge between carbon electrodes, he discovered a range of molecules that have been the object of intense scientific research ever since [1]. Using a high-resolution transmission electron microscope he found long molecules consisting of several coaxial cylinders of carbon. Multiwall carbon nanotubes, as they are known now, consist of carbon alone and have an outer diameter of a few nm. Two years after the discovery of multiwall carbon nanotubes, researchers found ways to synthesize even smaller tubes of one shell only which were coined singlewall carbon nanotubes [2]. Due to their small size and the special features of the carbon atom, both varieties of nanotubes exhibit some extraordinary properties.

Perhaps the most remarkable one is that the individual shells of a nanotube are 1-dimensional conductors that can be either semiconducting or metallic on the basis of geometrical factors alone. The mechanical properties are no less amazing and carbon nanotubes are simultaneously extremely strong and flexible fibres [3]. Due to this rather exceptional combination of properties, carbon nanotubes are now a model example of a robust 1-dimensional system. An additional advantage of nanotubes is that their extended lengths facilitate the use of standard electron beam lithography for device fabrication. This has been exploited in this thesis which describes electrical transport experiments on individual multiwall carbon nanotubes. These studies provide information on some basic electronic properties of the nanotubes such as the number of conduction channels or the amount of scattering electrons experience. In most experiments, however, the multiwall carbon nanotubes are primarily used as a well-defined model system and the observed transport characteristics are not nanotube specific but generic features of many mesoscopic devices. These include electron interference phenomena, quantum dot physics, and the effect of superconducting proximity.

1.1 Quantum interference phenomena

Electron transport in mesoscopic devices is often considered as a scattering problem. In this approach, the current through a conductor is related to the probability that an electron can be transmitted through it. This is expressed in the Landauer formula which relates the conductance G to the number of transmitting modes M in the conductor and the average transmission probability T of the modes [4, 5]:

$$G = \frac{e^2}{h} MT \tag{1.1}$$

where e^2/h is the conductance quantum. The contacts to the conductor are incorporated in this formula. This implies that even a ballistic conductor with a transmission probability of unity ($T = 1$) and perfect contact coupling has a finite resistance. For an ideal (i.e. undoped and ballistic) carbon nanotube, the expected 2-terminal conductance is $4\,e^2/h$ because there exist 2 spin-degenerate modes at the Fermi energy (see section 2.2). In general, additional scattering takes place at the contacts and in the nanotubes. An example of a scattering process is shown schematically in Fig. 1.1 in which a path starts out in mode n in lead 1 and after a few elastic scattering processes, transmits to mode m in lead 2. Note that a lead in this context is a conceptual entity which carries M modes and provides an ideal connection between the electron reservoirs and the scattering region of a conductor. The restriction to classical trajectories is allowed if the separation between scattering events is much larger than the electron wavelength. The overall transmission amplitude from mode n to mode m can be expressed as the sum of the probability amplitudes A_i of all possible paths connecting mode n in lead one and mode m in lead two. The transmission probability T_{mn} is obtained by squaring the transmission amplitude [6]:

$$T_{mn} = \left| \sum_i A_i \right|^2 = \sum_i |A_i|^2 + \sum_{i \neq j} A_i A_j^* \tag{1.2}$$

The first term represents the sum of the probabilities of all the paths, while the second term is due to interference among the different paths.

A striking effect of quantum interference is to enhance the probability for backscattering in a disordered system in the metallic regime. This is the precursor of strong electron localization and has therefore become known as weak localization [7]. The probability that an electron will be transmitted or reflected from a mode m into mode n is obtained by squaring the sum of probability amplitudes, as has been done in Eq. 1.2. If the conductor

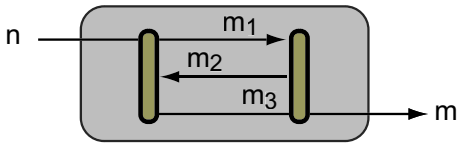

Figure 1.1: Example of a scattering process. A path starts out in an input mode n and finally leaves the conductor via an output mode m. Adapted from Ref. [8]

is phase-coherent, the second term of the equation describing the interference between the different paths cannot be neglected. However, usually the phases of the various paths are random and any interference effects cancel out on the (ensemble) average. This is correct if the beginning and end states are different. If the two coincide, i.e. for backscattered trajectories, one can group the sum of Eq. 1.2 in time-reversed pairs A_i^+ and A_i^-. Time-reversal invariance guarantees that the probability A^+ and A^- for clockwise and counterclockwise propagation around the closed loop are identical. The coherent backscattering probabilities $|A^+ + A^-|^2 = 4|A|^2$ is then twice the classical result. The enhanced probability for return to the point of departure reduces the diffusion coefficient and therefore the conductivity. The maximum weak localization correction turns out to be of the order of e^2/h, independent of the number of modes. For a diffusive metallic wire the correction is typically very small (compared to the background conductance) but the effect can be manifest dramatically in multiwall carbon nanotubes.

Another hallmark of quantum interference is the occurrence of so-called universal conductance fluctuations [6]. These are random sample-to-sample variations of the conductance of diffusive and phase coherent devices. Experimentally, universal conductance fluctuations are most conveniently studied in a single sample as a function of magnetic field or Fermi energy. The fluctuations depend on the specific scattering potential but are universal in the sense that their amplitude at zero temperature is of the order of e^2/h irrespective of the sample size and degree of disorder. A study of universal conductance fluctuations in MWNT devices is presented in section 4.4.

1.2 Quantum dot physics

The observation of quantum interference effects in small mesoscopic structures such as nanotubes requires a strong coupling to the electrical leads. More weakly coupled devices are in a transport regime which is often dominated by Coulomb interaction [9]. In these structures, the current is blocked when the charging energy U_C required for adding a single electron to the system is larger than the thermal energy available in the leads. However, electron transport can be restored if the energies of two charge states are degenerate. For example, an equilibrium current can flow via the sequence

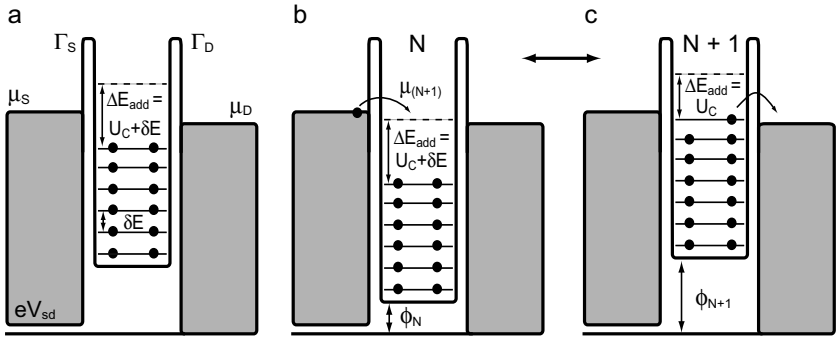

Figure 1.2: **(a)** Potential landscape of a quantum dot. The addition energy is larger than the energy available for electrons in the leads and the current is blocked. **(b-c)** When the electrostatic energy ϕ_N of the dot is lowered with a gate electrode, an electron can tunnel from the source electrode to the dot whereafter it can tunnel to the drain electrode.

$N \rightarrow N+1 \rightarrow N$ if the total ground-state energies for N and $N+1$ electrons are equal. Such degeneracies can be induced by adjusting the electrostatic potential with a capacitively coupled gate electrode.

In addition to the charging energy, the particle-in-a-box level spacing δE of the electron states needs to be taken into account. Devices in which electron transport occurs through individual quantum states are coined artificial atoms or quantum dots [10]. If the levels are spin degenerate, the addition energy required to add an electron to a quantum dot is given by $\Delta E_{add} = U_C + \delta E$ when the number of electrons is even and $\Delta E_{add} = U_C$ when the number of electrons is odd.

A schematic diagram of a quantum dot coupled to metallic leads is given in Fig. 1.2. The tunnel barriers that couple the dot to the source and drain electrodes are characterized by their tunnelling rates Γ. In the first diagram a situation is depicted in which electron transport is blocked. The addition energy is larger than the energy available for the electrons in the leads and the number of electrons will be a well-defined integer. In the second and third diagrams electron transport is restored. The gate voltage has been adjusted such that the electrostatic energy of the quantum dot is lowered and an electron level is aligned between the Fermi energies of the source and drain electrodes. The gate voltage required to lower the level will depend on the addition energy and the ratio between the gate and total capacitances. Electron transport can also be restored by applying a large bias voltage between the source and drain electrodes. The current will then increases

in steps each time a new level becomes available for transport (the excited states). The difference in the source-drain voltage ΔV_{sd} between the steps is directly proportional to δE. The study of the differential conductance as a function of gate and bias voltage thus provides important information on the electronic spectrum.

For a finite nanotube, the wave vector is quantized in the direction of the tube axis. The expected level spacing δE can then be calculated from the dispersion relation and the total effective length L of the tube. In the vicinity of the Fermi energy of an ideal nanotube, the single-electron level spacing is given by $\delta E = hv_F/2L$, where the Fermi velocity $v_F = 8 \cdot 10^5\,\mathrm{m/s}$. This implies that for a typical length of $L = 1\,\mu\mathrm{m}$ the level spacing is 1.7 meV. These are large energy scales and can be resolved in a standard He^4 cryostat (an energy of 1.7 meV corresponds to about 20 K). For an ideal tube the electron levels are four-fold degenerate (including spin) because of an additional orbital degeneracy of the 1-dimensional subbands of the nanotubes. In chapter 5 an experimental observation of the four-fold degeneracy in a multiwall carbon nanotube quantum dot is presented. This chapter also discusses higher-order tunneling processes which have been neglected in this short introduction.

1.3 Andreev reflection in mesoscopic devices

A superconductor does not have a continuous conduction band at the Fermi energy and an energy 2Δ has to be provided by a voltage source if a single electron is to be transferred between two superconducting reservoirs in their ground state, see Fig. 1.3a. A current can still flow at lower bias if higher-order processes are allowed to contribute. An incoming electron can be transferred into a superconductor if a second electron is also transferred through the interface to form a Cooper pair [11]. This process is equivalent to the reflection of a hole and goes under the name of Andreev reflection [12]. The electron transport involves a multiple of such Andreev reflections if the applied bias is small [13], see Fig. 1.3c. In general, the current between two superconductors, separated by a barrier characterized by a transmission probability T, is dominated by an Andreev process of order n determined by the applied bias as:

$$2\Delta/en \leq V_{sd} \leq 2\Delta/e(n-1) \tag{1.3}$$

The probability of higher-order Andreev processes is proportional to T^n when the transmission probability is small. The resulting I-V characteristics are therefore highly non-linear and often present a series of sharp current steps at the onset of each successive Andreev process.

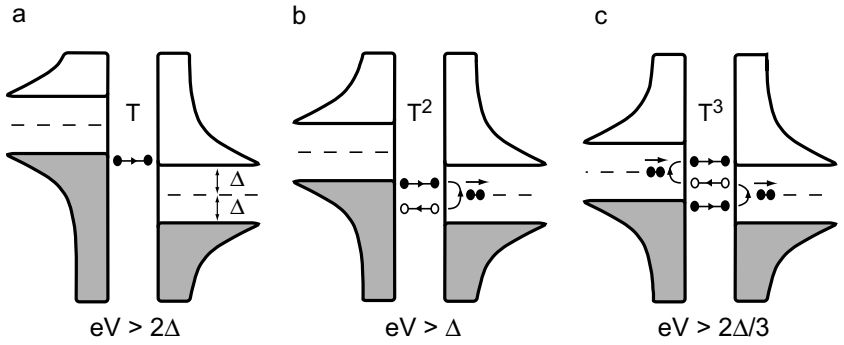

Figure 1.3: **(a)** Schematics of two superconductors coupled by a barrier with transmission probability T. At $V_{sd} > 2\Delta$ quasi-particles can tunnel directly from occupied states in the source to unoccupied states in the drain electrode. **(b)** First-order Andreev reflection. The solid and open circles represent quasi-particles and quasi-holes respectively. **(c)** Second-order Andreev reflection.

The observation of multiple Andreev reflection is not limited to tunnel junctions (as in Fig. 1.3) but can be observed in a number of systems where two superconductors are coupled by a weak link. Outstanding systems in this regard are atomic-size break junctions [14, 15]. Here the constriction of a single atom between two superconducting reservoirs restricts the number of conduction channels of the device to the number of available valence orbitals of the specific atom. The transmission probability of each channel is determined by the material and the exact atomic arrangement of the junction. In their turn, the observed I-V characteristics depend in a highly non-linear fashion on the transmission probability T of each mode. These measurements are therefore very useful as a tool to determine the set of transmission probabilities that make up the conductance.

The central atom of an atomic-size break junction is strongly coupled to its neighbours. Therefore, the discrete energy levels of the atom broaden to form a continuous density of states and it is for the same reason that electron-electron interaction can be neglected in these devices. In chapter 7 of this thesis we investigate a novel system of two superconductors coupled by a multiwall carbon nanotube quantum dot which can be considered as an artificial atom. As discussed in the previous section, size and charge quantization cannot be neglected in quantum dots. This has a pronounced effect on the transport properties, both when the reservoirs are in the normal state (in the presence of a small magnetic field) and when the leads are superconducting. An advantage of quantum dots is that the presence of a

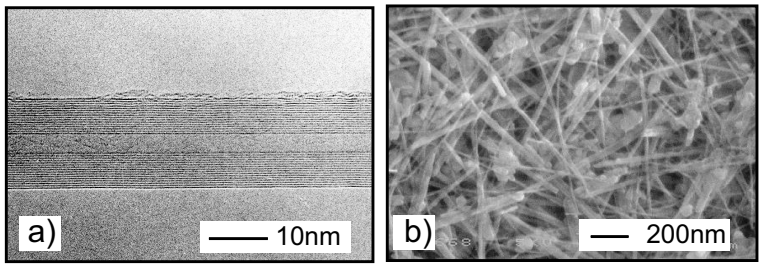

Figure 1.4: **(a)** TEM image of a multiwall carbon nanotube synthesized by the arc-discharge method. The individual shells of the nanotube are clearly visible. **(b)** SEM image of a powder of purified multiwall carbon nanotubes.

gate electrode allows one to adjust the level position of the single-electron states and to study the system in a number of different configurations. For example, the total spin on the quantum dot can be varied between 0 and 1/2. This has been exploited in chapter 7 which emphasizes the interplay between the Kondo effect in quantum dots and superconductivity. Moreover, the observed multiple Andreev reflection pattern is compared with a theoretical model of the device.

1.4 Multiwall nanotube material and devices

All transport experiments described in this thesis have been on multiwall carbon nanotubes (MWNT) with outer diameters between approximately 5 and 15 nm. The length of the MWNTs can be many μm's. Figure 1.4 shows a SEM image of a powder of MWNTs and a TEM image of an individual MWNT produced by Laszlo Forró's group at the EPFL (Lausanne) from whom we have obtained the MWNT material. The tubes have been synthesized by the arc-discharge method [1, 16, 17]: a current of order 100 A is passed through a graphite rod (anode) to a graphite cathode in a He atmosphere. A deposit forms on the cathode containing bundles of MWNTs. Singlewall nanotubes (SWNTs) can also be produced by this method but this requires the addition of catalyst particles like Co or Ni which cannot be completely removed by purification methods. For MWNTs no catalyst particles are necessary and the tubes therefore do not contain any of these (magnetic) impurities. Furthermore, high-resolution TEM images have shown that arc-discharge grown MWNTs contain very few defects. The as-grown material, however, is often covered by a thin layer of amorphous carbon. Furthermore, it is exposed to ambient conditions (containing e.g. O_2, H_2O) which may effect the electrical transport properties of the tubes (see also

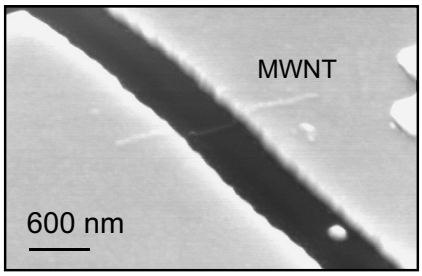

Figure 1.5: Scanning electron microscope image of an individual MWNT on an oxidized Si substrate and contacted by two Au reservoirs. The tube is lying completely *under* the reservoirs. On the right, (part of) an alignment marker is still visible.

chapter 3). The MWNT material has been stored in chloroform.

To make electrical contact to individual MWNTs, a droplet ($\sim$ 50 μl) of the suspension of nanotubes in chloroform is deposited on an oxidized Si wafer (2 x 2 cm) with pre-defined alignment markers and bonding pads. Prior to deposition, the dispersion is sonicated for several minutes. Directly after the droplet has spread, the wafer is rinsed with isopropanol (IPA) and dried in a N_2 flow. Next, the MWNTs are imaged in an SEM (Philips XL30 FEG, 15 kV acceleration voltage) in order to locate the randomly deposited tubes. Only individual tubes are selected. After having noted the coordinates of the tubes with respect to the alignment markers a layer of polymethylmethacrylate (PMMA) resist is spun over the wafer. Electron beam lithography (Jeol JSM-IC848 SEM, 35 kV acceleration voltage) is used to pattern the contact structure into the resist. The exposed PMMA is then removed with a developer (MibK:IPA in a ratio 1:3) and rinsed with IPA after 45 seconds to stop the development. The metal deposition (usually Au and/or Al) has been done by e-beam evaporation in a Balzers PLS 500 system. The e-gun is equipped with four revolving targets which allows for the evaporation of different materials without breaking the vacuum (typically 10^{-7} mbar). Usually the sample was cooled ($\sim 0^\circ$ Celsius) during evaporation. Figure 1.5 shows an example of a contacted MWNT. The electrical contacts to the tube terminate as large bonding pads on the wafer (not shown). A finished device is mounted in a commercially available chip carrier and contacted with the use of an ultrasonic bonding machine

Chapter 2

Theoretical background on carbon nanotubes

2.1 Geometric structure

A carbon nanotube can be considered as a graphene sheet that is rolled up into a seamless cylinder. One of the many possible realizations is shown in Fig. 2.1. Each tube is uniquely defined by the vector $\mathbf{C}=n\mathbf{a}_1+m\ \mathbf{a}_2$, where $\mathbf{a}_1$ and $\mathbf{a}_2$ are the unit vectors of the hexagonal lattice. The pair of indices (n, m) corresponds to a specific set of chiral angle ϕ and diameter d:

$$\phi = \arccos[\sqrt{3}(n+m)/2\sqrt{n^2+m^2+nm}] \tag{2.1}$$

$$d = \frac{a}{\pi}\sqrt{n^2+m^2+nm} \tag{2.2}$$

where $a = 2.46\,\text{Å}$ is the lattice constant. The unit cell of each tube is defined by the vectors $\mathbf{C}$ and $\mathbf{T}$. Special symmetry directions in the graphene lattice are $(n, 0)$ and (n, n) which are called the zigzag and armchair direction respectively. The names refer to the patterns of the carbon bonds around the circumference of the tube. Figure 2.2 shows examples of an armchair, a zigzag and a chiral tube together with a scanning tunnelling microscopy image of an individual single-wall carbon nanotube [18].

2.2 Energy dispersion of graphene and nanotubes

The dispersion relation of carbon nanotubes can be obtained from that of graphene which will, therefore, be discussed first. Figure 2.3 shows a fragment of the hexagonal graphene sheet in real and in reciprocal space. Each carbon atom in the graphene sheet has four valence electrons. Three electrons form a strong sp^2 σ-bond with its three nearest neighbours which

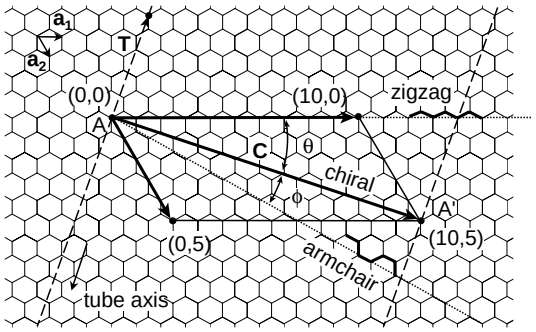

Figure 2.1: A graphene sheet is rolled up to form a (10,5) nanotube by connecting the dashed lines along vector C. The wrapping angle of chiral tubes are specified relative to the zigzag (θ) or armchair ($\phi = 30^\circ - \theta$) direction. Also shown is the lattice vector T of the 1D unit cell.

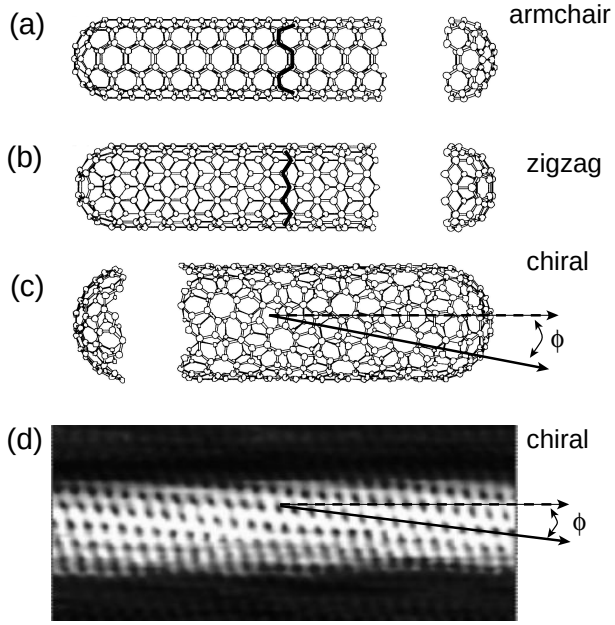

Figure 2.2: **(a-c)** Shown are a (5,5) armchair tube, a (9,0) zigzag tube, and a (10,5) chiral tube which has been constructed in Fig. 2.1. **(d)** Atomically resolved STM image of an individual single-wall carbon nanotube. The diameter here was found to be $d = 1.3$ nm and the chiral angle $\phi = 7^\circ$. Adapted from Ref. [18]

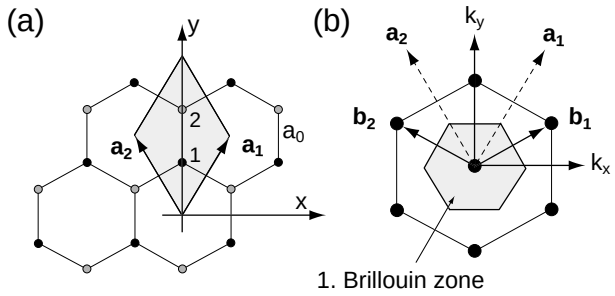

Figure 2.3: **(a)** Fragment of the graphene lattice. The primitive lattice vectors $\mathbf{a}_1$ and $\mathbf{a}_2$ define the unit cell (shaded). There are two carbon atoms per unit cell, denoted by 1 and 2. **(b)** Reciprocal lattice of graphene with the 1st Brillouin zone (shaded). The primitive lattice vectors are $\mathbf{b}_1$ and $\mathbf{b}_2$.

are in the same plane with angles of 120°. The fourth electron is in a π-orbital which has its lobes perpendicular to the plane of the sheet. The electronic properties of graphene and carbon nanotubes are well described taking into account the energy dispersion of the π-electrons only [19, 20, 21]. Note that the unit cell in real space of graphene contains 2 carbon atoms.

The dispersion relation for the π-electrons of the graphene sheet can be calculated in a tight-binding approximation yielding a bonding (-) and anti-bonding (+) band given by [22]:

$$E(k_x, k_y) = \pm\gamma_0 \left[1 + 4\cos\left(\frac{\sqrt{3}k_x a}{2}\right)\cos(\frac{k_y a}{2}) + 4\cos^2(\frac{k_y a}{2}) \right]^{1/2} \qquad (2.3)$$

where γ_0 is the energy overlap integral between nearest neighbours. The bandstructure is shown in Fig. 2.4. Note that the bonding and anti-bonding bands touch at 6 points that coincide with the corners of the hexagonal Brillouin zone. The Fermi surface is thus reduced to six points, two of which, the K and K' points, are inequivalent. The others can be obtained by lattice transformations along $\mathbf{b}_1$ and $\mathbf{b}_2$. In a carbon nanotube the electrons are free to move only in the length direction. To obtain the dispersion relation for a carbon nanotube, the quantization condition for the wavevector component along the circumference has to be included: $\mathbf{k} \cdot \mathbf{C} = 2\pi m$, where $m \in \mathbf{Z}$. In reciprocal space this quantization can be represented as parallel lines in the direction of the tube axis, see Fig. 2.5a for an example of a (10,10) armchair nanotube. Since the allowed k-lines cross the K and K' points (where the bonding and anti-bonding bands touch) this nanotube is metallic. The bandstructure of a (10,10) armchair nanotube is plotted in Fig. 2.5b. Each band is doubly degenerate, except for the ones crossing $E = 0$ and the ones with maximal and minimum energy. Near $E = 0$

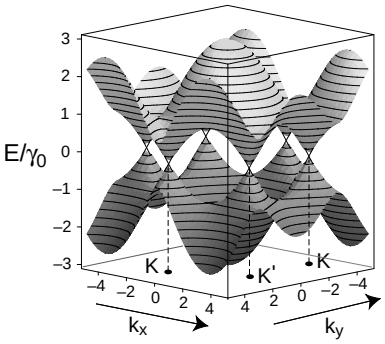

Figure 2.4: Bandstructure of graphene. The energy overlap integral between nearest neighbours $\gamma_0 = 2.5\,\mathrm{eV}$. Note that the the Fermi surface is reduced to six points.

the subbands are approximately linear with k_x and the energy dispersion is given by $E = \hbar v_F k_x$, where v_F is the Fermi velocity. Note that since the K and K' points are inequivalent, there are two sets of (spin-degenerate) propagating modes at the Fermi energy. The existence of two sets of spin-degenerate propagating modes is of importance for the interpretation of the electronic spectrum of MWNT quantum dots presented in chapter 5.

Armchair carbon nanotubes are always metallic whereas zigzag or chiral nanotubes can be either metallic or semiconducting. The interline spacing Δk depends only on the diameter as $d/2$. Since the distance between the center and edge of a hexagon in reciprocal space equals $2\pi/\sqrt{3}a$, see Fig. 2.5a, it follows directly from Eq. 2.2 that any (n,n) armchair nanotube is metallic. The different chirality of zigzag and chiral nanotubes means that the allowed k-lines for these nanotubes are rotated (by 30 degrees for zigzag nanotubes) and orientated differently around the K points. Zigzag and chiral tubes will be metallic if the allowed k-lines do cross the K points and semiconducting otherwise. The size of the energy gap of semiconducting nanotubes and the subband spacing of both semiconducting and metallic nanotubes is inversely proportional to the diameter [23]. A multiwall carbon nanotube typically consists of a concentric set of nanotubes of both varieties.

2.3 Backscattering in carbon nanotubes

Of interest for electronic transport experiments on carbon nanotubes is the amount of backscattering the electrons experience. An example of a backscattering processes, i.e the transition from a right moving state to a left moving one or vice versa, is shown in Fig. 2.6 which displays the energy dispersion in the vicinity of a K point for a metallic and semiconducting nanotube. In Fig. 2.6 the Fermi level is shown below the K and K' points in the valence or bonding bands. This is the situation observed in most

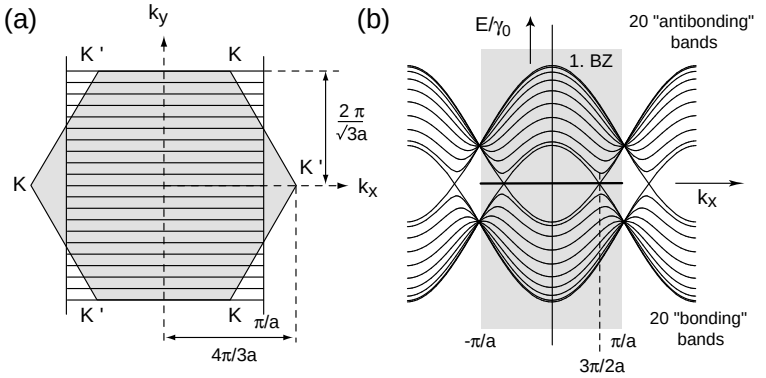

Figure 2.5: **(a)** Reciprocal space for a (10,10) armchair carbon nanotube. The parallel lines represent the allowed and independent k-values. **(b)** The corresponding bandstructure of the (10,10) armchair nanotube. The shaded region is the 1. Brillouin zone.

nanotube experiments and is the result of chemical or electrostatic doping. To estimate the scattering probability, it is important to realize that the unit cell of graphene contains 2 atoms each having one electron in a π orbital, see Fig.2.3. The atomic wavefunction $\phi(\mathbf{x})$ is therefore described by a linear combination of the electronic orbitals on the two sublattice atoms as:

$$\phi(\mathbf{x}) = s_1\phi_1(\mathbf{x}) + s_2\phi_2(\mathbf{x}) \tag{2.4}$$

where s_1 and s_2 give the amplitudes of the electronic wavefunctions on the carbon atoms. It now turns out that, in the vicinity of K (or K') and in addition to their real spin, the electrons possess a pseudospin, the two-component vector (s_1, s_2), see Refs. [24, 25, 26]. When considering backscattering processes, this pseudo-spin part of the wavefunction has to be taken into account. It can be shown that the matrix element between states depends on the angle between them as $\cos^2(\frac{1}{2}\ \theta_{k,k'})$, where k and k' are the initial and final states as in Fig. 2.6. As can be seen in the schematics, this angle for metallic tubes is π and such a process is not allowed. In other words, the k and k' states are built from an anti-bonding and a bonding molecular orbital respectively and are orthogonal. Interband scattering is still allowed but the direction of motion is retained in this process and does not introduce any electrical resistance. Metallic carbon nanotubes are therefore expected to have long mean-free paths. For semiconducting nanotubes the situation is different and, as the angle between initial and final states $< \pi$, backscattering is only partially suppressed.

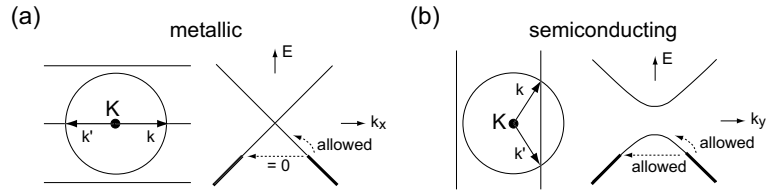

Figure 2.6: **(a)** Reciprocal space and energy dispersion for a hole-doped metallic carbon nanotube in the vicinity of a K point. The circle represent the Fermi surface of a hole-doped graphene sheet and the parallel lines represent the allowed k-values for the nanotube, as in Fig. 2.5. Interband scattering processes are suppressed (see text). **(b)** Same as panel (a) for a semiconducting nanotube. Both interband and intraband scattering processes are allowed. Adapted from Ref. [26].

Semiconducting nanotubes are therefore expected to be much more sensitive to (long-range) disorder as introduced by, e.g. dopant impurities. Note that by a simple extension of these arguments, the same would be true for the higher subbands of a doped (metallic or semi-conducting) nanotube. The amount of doping in multiwall carbon nanotubes is the topic of chapter 3.

Chapter 3

Doping state of multiwall nanotubes

Carbon nanotubes, in particular SWNTs, are prototype one-dimensional conductors which ideally come in two forms, either as metals or semiconductors. This classification assumes that nanotubes are undoped. An important parameter is the position of the Fermi energy E_F (the chemical potential) with respect to the charge neutrality point. For an undoped nanotube E_F coincides with the charge neutrality point. Electron (n) or hole (p) doping shifts the Fermi energy up or downwards. If the doping induced Fermi level shifts are larger than the energy separation between the 1D subbands, a semiconductor nanotube is turned into a metallic one. In previous work on SWNTs the characteristic 1D density-of-states was measured, from which $E_F < 0$ was deduced [18, 27, 28]. Hole-doping was also inferred from nanotube-based field-effect transistors [29, 30]. In contrast to semiconductor SWNTs, only weak field effects were observed in MWNTs [30].

3.1 Electrochemical carbon nanotube FET

Here we explore the electrochemically induced field-effect of carbon nanotubes. The electrochemical gating is so effective that E_F can be determined unambiguously on a single MWNT. An extreme sensitivity of the net doping concentration on the environment, in our case different electrolytes, is observed. Because the doping is reflected in the measured electrical resistance, nanoscaled sensors, such as pH sensors can be envisaged.

Electrochemical gating is studied on an individual MWNTs with lithographically defined Au contacts evaporated over the nanotubes [31]. The nanotube - contact structure is fabricated on degenerately doped Si with a

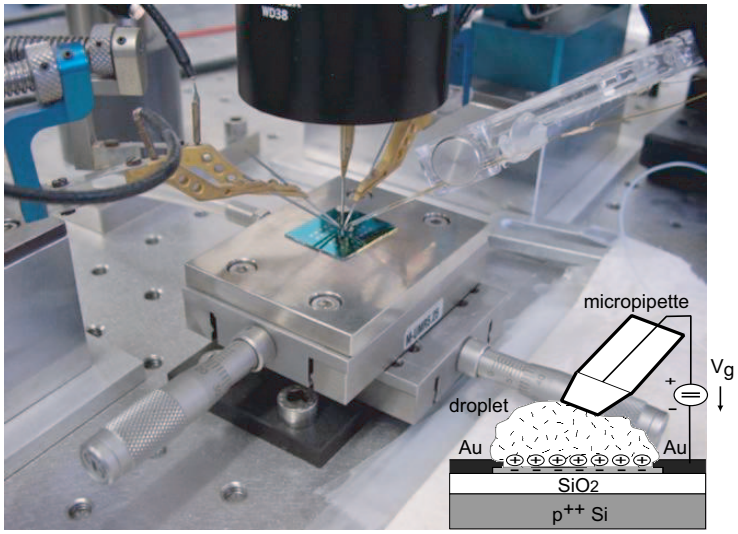

Figure 3.1: Liquid-ion gating of a MWNT.

400 nm thick SiO_2 spacer layer. The Si substrate can be used as a backgate. Large changes have been observed in the electrical resistance R of SWNT based field-effect transistors (FET) by using such a backgate. The transconductance can be increased if the gate is placed as close as possible to the nanotube, ultimately into intimate contact. This is achieved in the present work by immersing the nanotube into an electrolyte (Fig. 3.1). The resistance of the nanotube devices is measured on a probe stage at room temperature. The stage is complemented with a micropipette ending in a drawn glass capillary. The pipette is positioned over the device and a small droplet of size $\lesssim 100\,\mu$m is delivered. The droplet size is chosen such that the macroscopically large bonding pads are not immersed in the liquid resulting in negligible leak currents in the resistance measurements. The gate contact is formed by a Pt wire within the glass pipette. If, as sketched in the inset of Fig. 3.1, a positive gate voltage V_g is applied, the nanotube-electrolyte interface is polarized by the attraction of cations. The gate capacitance C_g is formed by the double-layer capacitance which can be very large. Here, we focus on experiments in $LiClO_4$ electrolytes, used at concentrations of 1-500 mM.

Figure 3.2 compares the gate effect of a MWNT for two cases: with (a) liquid ion-gate and (b) backgate. While the initial electrical resistances R at $V_g = 0$ are comparable, the gate induced changes are very different; dR/dV_g is $2.5\,\Omega$/V in (a) and $570\,\Omega$/V in (b). Hence, liquid-ion gating is by

a by a factor > 200 more effective than back gating. Starting from $V_g = 0$, R increases with increasing V_g, which is characteristic for p-type behavior. With the backgate, this increase persists up to the largest possible gate voltages of $\sim 80\,\mathrm{V}$, where the sample is destroyed. In contrast, $R(V_g)$ has a maximum at $V_g = V_0$ in the electrolyte. The decrease of R for $V_g \geq V_0$ now suggests n-type behavior. The position of the resistance maximum therefore marks the charge-neutrality point of the nanotube, i.e. $E_F = 0$, if $V_g = V_0 \approx 1\,\mathrm{V}$. The resistance $R(V_g)$ is measured cyclicly. After some cycles, an equilibrium situation is established with a relatively well-defined peak position and only weak hysteresis, provided one ramps slowly (10 min per sweep). In this example, R changes by only 20%.

Figure 3.3 shows another example. It illustrates the time dependence and, most notably, shows a much larger R change. The maximum resistance R_{max} is a factor of 5 larger than $R(0)$. Of all our measured samples, approximately half display a weak R change of order $20\% - 50\%$, whereas R changes by several 100% for the other half. The first up sweep (increasing V_g), shown as ($\times$) was followed by a down sweep (+). This is repeated until a stationary curve is obtained ($\bullet$). It is seen that the resistance maximum shifts to higher voltages with time to finally reach $V_0 = 1\,\mathrm{V}$ in this case.

In the following we will present a model which captures the essential physics of this experiment. We assume that only the outermost nanotube shell needs to be considered [32] and describe the nanotube DOS by that of a single layer of graphite, neglecting 1D bandstructure effects [3]. This is justified, because $k_B T$ is of order of the subband separation at room temperature. Using the Einstein relation, which relates the diffusion coefficient D to the conductivity, the electrical conductance G can be written as $G = (2\pi r/L)e^2 D N_\square$. Here, r is the radius of the nanotube, L the contact separation, and $N_\square$ the two-dimensional DOS which depends on E_F. For an ideal single sheet of graphite, the DOS is $N_\square = 2|E_F|/\pi(\hbar v_F)^2$, where v_F is the Fermi velocity. At the charge-neutrality point, i.e., at $E_F = 0$, $N_\square$ vanishes. We add a phenomenological parameter E_C accounting for a finite DOS at the CNP due to temperature and adsorbate induced bandstructure modifications and write $N_\square = (2E_C/\pi(\hbar v_F)^2)(1 + (E_F/E_C)^2)^{1/2}$. The normalized conductance $g(E_F) = G(E_F)/G(0) = (1 + (E_F/E_C)^2)^{1/2}$ is used to fit our data. For this $g(V_g)$ is required, so that the relation between V_g and E_F needs to be derived.

Figure 3.4 shows schematically what happens when a nanotube is biased via an external gate (engineering sign convention is used here). There are two effects: Firstly, there is an external electric field $\overrightarrow{E}$ and correspondingly an electrostatic potential difference ϕ between the nanotube and the gate electrode. Secondly, E_F must increase because of the addition of charge carriers to the nanotube. The relation between charges Q_1, Q_2, (see

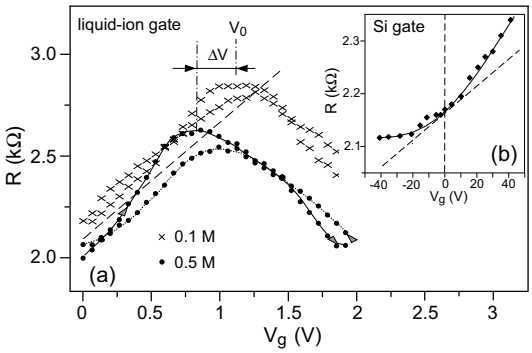

Figure 3.2: Electrical resistance R of a MWNT as a function of gate voltage V_g measured **(a)** in a $LiClO_4$ electrolyte for two ion concentrations (0.1 and 0.5 M) and **(b)** in air with a backgate.

Fig. 3.4c) and potentials $E_F/e, \phi$ are determined by the geometrical capacitance $C_g = dQ_2/d\phi$ and chemical capacitance $C_{NT} = dQ_1/d(E_F/e)$ of the nanotube (NT), see Fig. 3.4c. These two capacitors are in series. Figure 3.4b. shows the energy-dependent DOS for a general biasing condition. The externally applied voltage V_g corresponds to the electrochemical potential η, given by $eV_g = \eta = E_F + e\phi$. From this relation together with $dQ_1 = dQ_2$ and C_g, C_{NT} we obtain

$$e\frac{\partial V_g}{\partial E_F} = 1 + \frac{C_{NT}(E_F)}{C_g}, \tag{3.1}$$

which provides us with the required relation between V_g and E_F. A significant simplification follows for nanotubes immersed in electrolytes because $C_g \gg C_{NT}$. This is shown now. The differential nanotube capacitance per unit length (denoted by C' instead of C) is given by $C'_{NT} = e^2 N'(E_F)$ with $N'(E_F) = 2\pi r N_\Box(E_F)$. Thus, $C'_{NT} = C'_0(1 + (E_F/E_C)^2)^{1/2}$ with $C'_0 = 4e^2 r E_C/(\hbar v_F)^2$. Taking $r = 5\,\text{nm}$, $v_F = 10^6\,\text{m/s}$, and $E_C = 0.1\,\text{eV}$ one obtains $C'_0 \approx 100\,\text{pF/m}$. The gate capacitance in solution (the double layer capacitance) is $C'_g = 2\pi r\epsilon/\lambda$, where ϵ is the dielectric constant ($\epsilon_{H_2O} \approx 80 \times \epsilon_0$), r the nanotube radius, and λ the screening length $\propto c^{-1/2}$ (c = ion concentration). Taking $c = 0.1\,\text{M}$, typical numbers are $\lambda \approx 1\,\text{nm}$ and $C'_g \approx 10\,\text{nF/m}$. If the nanotube is gated by the Si substrate, a coupling capacitance of $C'_g \approx 5\,\text{pF/m}$ is deduced from our experiments (valid for 300 nm contact separation). Hence,

$$C_g(\text{BG}) \ll C_{NT} \ll C_g(\text{electrolyte}). \tag{3.2}$$

If the nanotube is immersed in an electrolyte, the case of interest here,

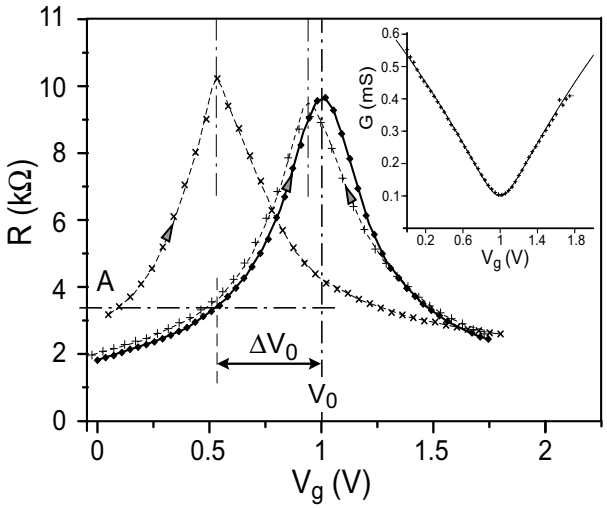

Figure 3.3: Electrical resistance $R(V_g)$ of a MWNT measured in a 10 mM $LiClO_4$ electrolyte. After immersion, the measurement commenced at point A with the data-point sequence $\times, +, \bullet$ (10 min per curve). Drawn curves are guides to the eye. Inset: Comparison of $G = 1/R$ ($\bullet$) with theory (full curve).

the gate capacitance is much larger than the internal nanotube capacitance and we obtain from Eq. 3.1 a very simple relation $eV_g \simeq E_F$, valid for an undoped nanotube. If it is doped, $Q_2 \neq Q_1$. We denote the doping charge by $Q_d = Q_2 - Q_1$ and the external gate voltage required to induce charge neutrality by V_0. Since $E_F = 0$ at the CNP, $V_0 = Q_d/C_g$. The effect of doping is simply to shift the functional dependence of E_F versus V_g, so that $E_F \simeq e(V_g - V_0)$. The interpretation of the measured two gate sweeps is now straightforward because there is a one-to-one correspondence between V_g and E_F. V_0 coincides with the CNP and directly reflects E_F for an unbiased nanotube (in the engineering convention $E_F > 0$ corresponds to an excess of positive carriers). A substantial hole doping for MWNTs immersed in $LiClO_4$ is evident, leading to Fermi level shifts of $\sim 1\,\mathrm{eV}$. What is the origin of this considerable hole doping ?

Figure 3.2a. shows two measurements of the same MWNT for $c = 0.1$ and $c = 0.5\,\mathrm{M}$. If we assume that doping is intrinsic to the nanotube, for example due to defects or inclusions, the doping charge Q_d should be constant. The relation $V_0 = Q_d/C_g$ predicts that the position of the resistance maxima should shift to lower values with increasing c according to $V_0 \propto c^{-1/2}$. Though a peak shift in the right direction is seen in Fig. 3.2a, the magnitude is far too low, suggesting that Q_d is affected by the electrolyte itself.

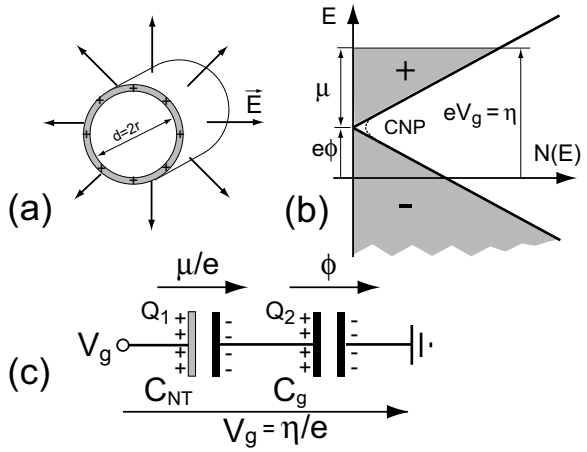

Figure 3.4: **(a)** Single sheet nanotube is assumed to model $R(V_g)$. **(b)** The energy-dependent DOS under a general biasing condition. CNP denotes the charge-neutrality point, ϕ, E_F, and η the electrostatic, chemical, and electrochemical potentials. **(c)** A geometrical (C_g) and chemical (C_{NT}) capacitance need to be considered to account for the dependence of $E_F(V_g)$.

This conclusion is supported by the time dependence shown in Fig. 3.3. If the nanotube is immersed into the electrolyte the resistance $R(V_g = 0)$ drops which corresponds to a shift of V_0 to the right. During the first sweep in Fig. 3.3, $V_0 \simeq 0.5\,\mathrm{V}$, whereas $V_0 \approx 1\,\mathrm{V}$ in all later sweeps. It is clear that $E_F < 0.5\,\mathrm{eV}$ in air before immersion. Hence, we conclude that the electrolyte induces hole doping in the nanotube, the magnitude of which depends on c. Intercalation of Li-ions can be excluded because this would lead to n-doped nanotubes. This leaves the perchlorate ion ClO_4^- as the source of doping. This (weakly) oxidizing species seem to adsorb on the nanotube specifically leading to a charge transfer which partially oxidizes the nanotube (hole doping). It is evident that this oxidation is weak in the sense that the carbon network of the nanotube remains intact. If the nanotube would be eroded, irreversible measurements with a final loss of the conductance would be expected. If ClO_4^- is able to dope nanotubes by physisorption the same is expected from O_2 in air. A large sensitivity of the nanotube conductance on different kind of gases, in particular also O_2, have been reported recently [33, 34]. This scenario is further supported by our measurements in other electrolytes. If a a stronger oxidizing electrolyte is used, we observe an additional shift of the $R(V_g)$ curve to the right (additional hole doping). In contrast, the curve shifts to the left in a reducing

solvent.

Finally, a quantitative comparison of the experiments with theory is possible. This is demonstrated in the inset of Fig. 3.3 where a fit (taking the full theory) to the measured conductance G is shown. The fit yields: $E_C \approx 0.12\,\mathrm{eV}$ and $A \equiv C_g/C_0 \approx 10$. The product AE_C only depends on known parameters, like ϵ, v_F, and c, but not on the nanotube radius r. Our model predicts for this product 0.9 eV which is in good agreement with 1.2 eV obtained from the fit. This agreement proves that the model of a single tube is correct, implying that the electrical current flows preferentially in the outermost shell where most of the electrical field is screened. The parameter E_C was introduced to account for a finite DOS at the CNP. $N'(0)$ is found to be $\sim 6\times$ larger than N'_{1D} of an ideal metallic SWNT, possibly because of dopant induced states [35]. The other class of $R(V_g)$ curves, which show a much weaker resistance change [e.g., Fig. 3.2b] can be fitted too. However, the deduced parameters are inconsistent with the model of a single tube. In these cases, the current is most likely flowing in inner shells too, explaining the much weaker gate effect.

For the interpretation of previous electrical measurements, the net doping concentration Q_d and the Fermi-level shift for an as-grown MWNT in air are important. The later can immediately be obtained by comparing R_0 measured in air for $V_g = 0$ with the $R(E_F)$ dependence of the same nanotube. This is indicated in Fig. 3.3: the dash-dotted line corresponds to R_0 and ΔV_0 denotes E_F before immersion. Typical values are $0.3 - 0.5\,\mathrm{eV}$. Comparing this with the average 1D subband spacing $\hbar v_F/2d$ ($\approx 33\,\mathrm{meV}$ for a 10 nm diameter nanotube), we conclude that 9-15 subbands may contribute to G instead of 2 for an ideal metallic nanotube. This finding explains why previous low-temperature measurements could be fairly well described by 2D diffusive transport [31]. A doping-induced $E_F = 0.3\,\mathrm{eV}$ corresponds to a doping concentration of $Q'_d/e \approx 2 \times 10^3\,\mu\mathrm{m}^{-1}$ or, expressed per surface area, to $Q_d/e \approx 0.7 \times 10^{13}\,\mathrm{cm}^{-2}$ giving approximately one elementary charge per 500 carbon atoms. Finally, estimates for the diffusion constant D can be given too. We obtain $D = 170 \pm 50\,\mathrm{cm}^2/\mathrm{s}$ corresponding to a mean-free path of 35 nm, in agreement with our previous results obtained differently [31].

MWNTs in air are hole-doped with a (sheet) doping concentration of $\sim 10^{13}\,\mathrm{cm}^{-2}$ caused by the adsorption of oxygen. If immersed in a $LiClO_4$ electrolyte doping increases further most likely due to a specific adsorption of the oxidizing species ClO_4^-. Polarizing the nanotube via an electrolyte allows to move E_F over a wide range, resulting in large resistance changes. Nanotubes are possibly the most sensitive FETs for environmental application, because the mobile nanotube carriers are in intimate contact with the environment.

3.2 Fermi level shifts by local aluminum gates

The large shift of the Fermi energy with liquid-ion gating relies on the fact that the MWNT and electrolyte are in intimate contact. Disadvantages of this method are that the droplet applied cannot be made much smaller than $\sim 50\mu$m. Furthermore, the device cannot be left to itself (the droplet slowly evaporates), nor can it be cooled down to cryogenic temperatures. A close-by gate that circumvents these problems is a local gate of aluminum, only separated from the nanotube by a few nanometers of AlO_2. Schematics of two such devices that have been measured are depicted in 3.5. The aluminum is evaporated directly over the MWNTs. In practically all cases this did *not* introduce any electrical shorts and resistance values $\gg 10\,\mathrm{M}\Omega$ are standard (shorts could appear if the voltage difference between gate and tube exceeds more than ~ 4 V). It is conceivable that during evaporation (typical pressure 10^{-7} mbar) the aluminum reacts with oxygen residues or water on the tube, forming a thin oxide layer. Since Al is a reducing agent a peak shift of the resistance maximum to the left, towards the neutral state, might be expected. This has indeed been observed in a number of samples. Sometimes an even further shift to an n-doped state (as in Fig. 3.5) is seen. The devices are stable in time and it seems that the evaporation of Al protects the tube from adsorbing oxygen again and stabilizes a hole-depleted state. Similar to the electrochemical gating the nanotube can reversibly be tuned between a p and n-type device by changing the gate voltage. A similar use of local Al gates to tune the doping state of semi-conducting SWNTs between a p and n state has recently been reported in Ref. [36]. In this work, a range of logic operations has been demonstrated by integrating several SWNT devices on the same chip.

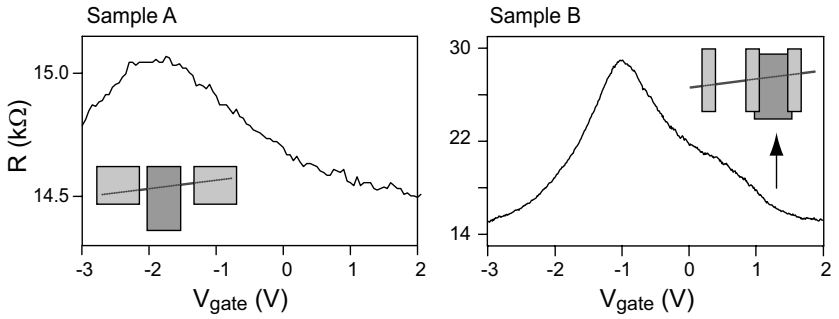

Figure 3.5: Shown are the resistance versus V_g at room temperature for two MWNT samples contacted with Au electrodes and covered by an Al gate (see schematics). The width of the Al gate is ~ 500 nm in both cases. The 2t-resistance curve of sample B is of the MWNT piece under the Al gate.

Chapter 4

Multiwall nanotubes as quantum wires

In the next two sections, low-temperature transport measurements on multiwall nanotube devices will be discussed. It is found that the phase-coherence length l_ϕ can be very large (of order 1 μm). Provided that the tubes are well coupled to their leads, the transport properties are dominated by quantum interference phenomena such as weak localization and universal conductance fluctuations.

4.1 Weak localization and AAS oscillations

A striking effect of quantum interference is to enhance the probability for backscattering in a disordered system in the metallic regime. This is the precursor of strong electron localization and has therefore become known as weak localization [7]. Weak localization can be suppressed by applying a magnetic field. The counter-propagating trajectories which are responsible for the weak localization correction to the conductance will acquire a phase difference in a magnetic field and no longer interfere constructively (see section 1.1). The longest paths which contribute to weak localization are those with a size approximately equal to l_ϕ and will give the largest phase-shifts at a given field. The critical field necessary to destroy weak localization depends on the value of the phase-coherence length and magnetoresistance measurements are therefore often used to probe l_ϕ.

In what follows, two sets of magnetoresistance measurements by Bachtold *et al* on MWNTs are reviewed [31, 32]. Figure 4.1a shows the magnetoresistance of a MWNT ($L = 1.9\,\mu$m) perpendicular to B for 5 different temperatures [31]. Note that the curves of Fig. 4.1a are not offset for clarity. A resistance maximum is observed at zero magnetic field. The resistance

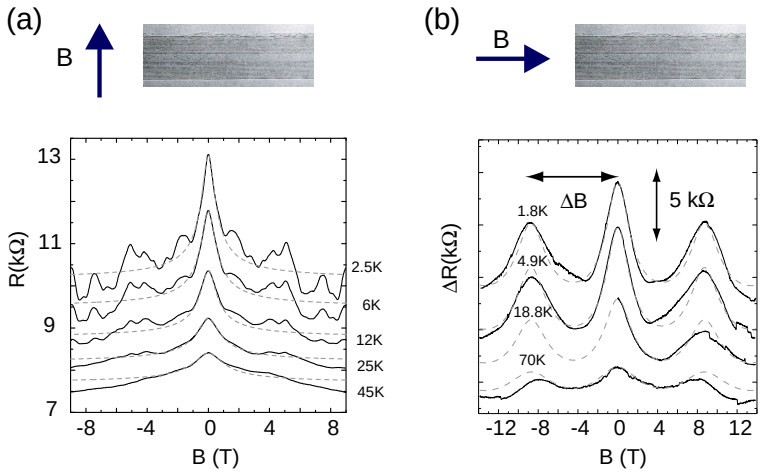

Figure 4.1: **(a)** Four-terminal magnetoresistance of an individual MWNT in perpendicular field for 5 temperatures. Note that the curves are *not* offset for clarity. The decrease of the resistance on applying a magnetic field is attributed to weak localization. The dashed curves show fits using 1D weak-localization theory. **(b)** Magnetoresistance measured for a MWNT in parallel magnetic field. The curves are offset. Due to the cylindrical shape of the MWNTs the weak-localization correction is periodically modulated with a magnetic-field period determined by the radius of the outermost shell of the MWNT. Adapted from Ref. [32]

decreases on applying a magnetic field. This is consistent with weak localization in a diffusive metallic conductor. The dashed curves are fits to 1D weak localization theory [31]. From these fits the coherence length can be deduced. The coherence length can also be estimated in a simple way. The weak-localization conduction correction δG_{WL} in a system that is 1D with respect to l_ϕ is of the order $(2e^2/h)(l_\phi/L)$. Comparing the conductance values at zero and high magnetic field (where weak localization is completely suppressed) directly yields δG_{WL} and therefore l_ϕ as the sample length L is known. At 2.5 K the conductance difference is $\sim 0.4\, e^2/h$ and the estimate for $l_\phi \sim (0.4/2) \times 1.9\,\mu\text{m} \approx 380\,\text{nm}$. This value is consistent with the more elaborate fit of the data to 1D weak-localization which yields $l_\phi \sim 500\,\text{nm}$. This also shows that the interference correction is indeed in the 1D limit, i.e. $d \ll l_\phi \ll L$, where d is the MWNT diameter.

The conductance at high magnetic field, when weak-localization is suppressed, is still found to be temperature dependent. This temperature dependent background conductance most probably results from residual electron-electron interaction (see also chapter 6). The aperiodic fluctua-

tions superimposed on the weak-localization curve are attributed to universal conductance fluctuations (UCF) and will be discussed in more detail in section 4.2.

Figure 4.1b shows the magnetoresistance of an individual MWNT aligned parallel to B measured for 4 different temperatures [32]. At zero magnetic field the resistance has a maximum. On increasing the magnetic field the resistance decreases. At $B \approx 8.8\,\mathrm{T}$, however, a second resistance peak develops. The resistance peak at zero field can be understood in the framework of weak localization. In the special case of a diffusive and thin-walled cylinder in a parallel magnetic field it encloses a well-defined flux and the weak localization correction to the conductance is periodically modulated with a magnetic-field period given by $\Delta B = (h/2e)/r^2\pi$, where r is the radius of the cylinder. This is known as the Altshuler-Aronov-Spivak (AAS) effect. Using this relation, a magnetic-field period of 8.8 T would correspond to a cylinder radius of $r = 8.6\,\mathrm{nm}$. This value is in excellent agreement with the outer radius $r_o = 8 \pm 0.8\,\mathrm{nm}$ of the MWNT as determined by atomic force microscopy.

Agreement with theory could only be obtained if at most two outer shells contribute to the current. This is much less than the number of shells that make up an actual MWNT (in this case ~ 20 are expected). If much more shells would contribute, no clear period could have been observed as the different shells have different diameters which would lead to a superposition of different periods. It can therefore be concluded that quantum-interference corrections to the resistance can account for the measured magnetoresistance, if and only if the electrical current is assumed to flow in one (or two) of the outermost shells. This is a crucial observation. It means that, as long as low-temperature, low-bias transport measurements are concerned, a MWNT can be considered as a large-diameter SWNT. These findings have been confirmed recently by Collins and co-workers who determined the contribution of each individual shell to the conductance directly by removing the carbon shells sequentially [37]. It was found that at low temperatures leakage currents through inner shells were frozen out, in accordance with the conclusions of the AAS interference measurement.

The observation of weak localization and of AAS oscillations in the magnetoresistance clearly shows that backscattering is present in MWNTs and that they are therefore *not* ballistic. How diffusive are the MWNTs ? The value of the mean free path could be estimated from a careful analysis of the temperature dependence of l_ϕ and turns out to be of order 100 nm for the MWNT in perpendicular magnetic field, Fig. 4.1a (see Ref. [31]). As this number is much larger than the tube diameter d but still smaller than the sample length transport should be qualified as quasi-ballistic rather than diffusive.

A shorter mean-free path l, however, is expected for the MWNTs showing AAS oscillations since this effect is based on interference of time-reversed trajectories due to scattering along the circumference of the tube, which requires $l \lesssim \pi d$. The microscopic origin of scattering is not known and this variation in mean-free paths may reflect a sample-to-sample variation in disorder potential by static impurities, scattering by inner shells or even of atomic defects. A large variation of mean-free paths is not unique for MWNTs but also observed for SWNTs. For SWNTs these differences arise from the different response of metallic and doped semiconducting tubes to disorder. As found in Refs. [24, 25, 26], backscattering by long-range disorder is suppressed in metallic tubes, in marked contrast to the semiconducting ones (see also section 2.3). An extension of these arguments shows that this also holds for backscattering in higher subbands, i.e. scattering is not suppressed for sufficiently doped carbon nanotubes (see also chapter 3). Analogous to SWNTs, the variation in l might therefore be the result of differences between semiconducting and metallic outermost shells and the degree of doping of the MWNTs.

4.2 Universal conductance fluctuations

Another fingerprint of quantum interference are universal conductance fluctuations (UCF) [38]. In a phase-coherent device the total conductance is given by the total transmission probability between source and drain electrodes. This, in turn, depends on the scattering potential, on the wavelength of the electrons at the Fermi energy, and on the phase-shifts induced by a magnetic field. Since in a diffusive (or quasi-ballistic) conductor the transmission probability will change randomly if these parameters are changed also the conductance fluctuates randomly from sample-to-sample, as a function of gate voltage, or as a function of magnetic field. The most surprising feature of UCF is that the magnitude of these conductance fluctuations (the root-mean-square value) at zero temperature is of the order e^2/h, regardless of the sample size and degree of disorder which are therefore called *universal* conductance fluctuations.

Magnetic field

Figure 4.2 shows the conductance of an individual MWNT as a function of magnetic field for 6 different temperatures. The sample has been contacted with 4 electrodes separated by 400 nm. The difference between 2 and 4-terminal resistance measurements is $\sim 1.5\,\mathrm{k}\Omega$ at all temperatures. This shows that the metallic electrodes are very well coupled to the MWNT

and Coulomb blockade therefore expected to be of minor importance. The conductance has a minimum at 0 Tesla for all temperatures and shows aperiodic fluctuations at higher fields. At the lowest temperatures these fluctuations completely dominate electron transport. Assuming that these features are due to electron interference, valuable information about the coherence length can be extracted. As before, the conductance minimum at $B = 0\,\mathrm{T}$ is attributed to a weak-localization correction to the conductance. From the weak-localization dip the coherence length at 8 K is estimated to be $\sim 50\,\mathrm{nm}$.

Also the amplitude of the universal conductance fluctuations can be compared with theory [38, 6]. Electron transport between source and drain is fully coherent if the coherence length equals (or exceeds) the sample length. In that case the root-mean-square value of the conductance fluctuations should saturate at a value of $\delta G_{rms} \approx 0.73\, e^2/h$. If time-reversal symmetry has been broken (for instance by a magnetic field) this equals $\delta G_{rms} \approx 0.52\, e^2/h$. The UCF amplitude at $T = 400\,\mathrm{mK}$ gives $\delta G \approx 0.40\, e^2/h$, close to the universal limit. This suggests that at these temperatures $l_\phi \approx L$ and that transport occurs through one phase coherent unit.

For smaller l_ϕ, the UCF amplitude is suppressed. The effect of $l_\phi < L$ is to subdivide the sample in uncorrelated segments of length l_ϕ. The conductance fluctuations of each individual segment will still be of order e^2/h. Except for the prefactor, δG_{rms} is then easily obtained if one calculates δG for L/l_ϕ uncorrelated segments in series:

$$\delta G_{rms} = C \frac{e^2}{h} \left(\frac{l_\phi}{L} \right)^{3/2} \tag{4.1}$$

where C is a constant which equals $\sqrt{12}$ if time-reversal symmetry applies and $\sqrt{6}$ when it is destroyed by a magnetic field. Note that the dependence of UCF on l_ϕ (and therefore on the temperature) is stronger than that of weak localization. Indeed the aperiodic fluctuations disappear faster in the experiment than the conductance dip at $B = 0\,\mathrm{T}$. The estimated δG_{rms} for $l_\phi = 50\,\mathrm{nm}$ at $T = 8\,\mathrm{K}$ yields $\sim 0.1\, e^2/h$ which is in good agreement with the experimental observations.

In Fig. 4.2b the values of δG_{rms}, evaluated at $B > 1.5\,\mathrm{T}$ and corrected for the weak localization slope, is given for all temperatures. The number of fluctuations is very limited. Nevertheless, the UCF amplitude seems to follow a powerlaw behavior in temperature. A best fit yields a slope of -0.55 ± 0.2. Following Eq. 4.1 this implies for the coherence length that $l_\phi \propto T^{-0.37}$. This result is mentioned because it is consistent with a number of similar measurements on other MWNT devices and with the temperature dependence of l_ϕ from fits to the weak localization correction at $B = 0$

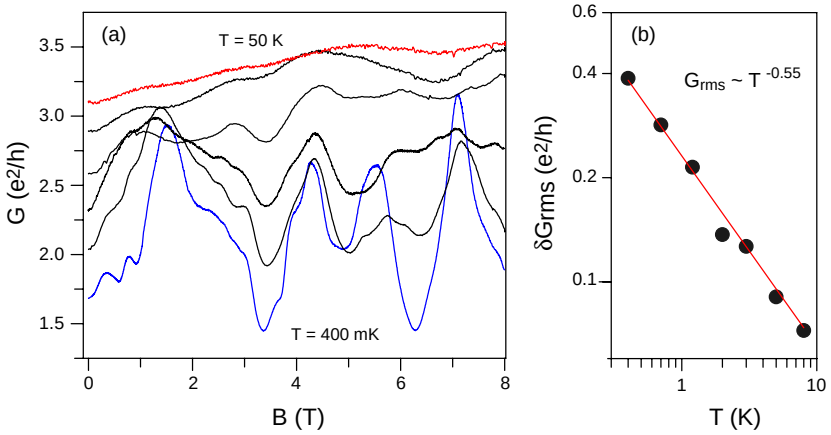

Figure 4.2: **(a)** Conductance versus perpendicular magnetic field at temperatures between 400 mK (blue) and 50 K (red). The distance between electrodes is 400 nm. On applying a field B the conductance increases in accordance with weak localization. This in best seen at high temperatures. At the lowest temperatures the curves are completely dominated by aperiodic conductance fluctuations, attributed to UCF. The magnitude of the fluctuations, δG_{rms}, reaches a value of $\sim 0.4\, e^2/h$ at 400 mK. **(b)** The corresponding root-mean-square δG_{rms} of the conductance fluctuations versus temperature.

T. For a wire that is 1D with respect to weak localization the dominant dephasing mechanism is by quasi-elastic electron-electron scattering, a process known as Nyquist dephasing [39, 40]. In this theoretical model the coherence length is expected to follow a $T^{-1/3}$ behavior, close to what has been observed for MWNTs.

Gate potential

Universal conductance fluctuations can also be studied by changing E_F by means of a gate electrode. Figure 4.3a shows a grey-scale representation of the differential conductance as a function of source-drain (V_{sd}) and gate voltage (V_g) for a 2.2 μm MWNT with short ($L = 300\,\mathrm{nm}$) contact spacing. A small magnetic field of $B = 150\,\mathrm{mT}$ is applied perpendicular to the tube axis. The linear-response conductance G and the corresponding root-mean square of the fluctuations δG_{rms} versus temperature are shown in Figs. 4.3b and 4.3c, respectively. Large and reproducible fluctuations of order e^2/h develop in G versus V_g. Note that the average conductance is quite large, i.e., $\langle G \rangle \sim 4.0\, e^2/h$ and temperature independent.

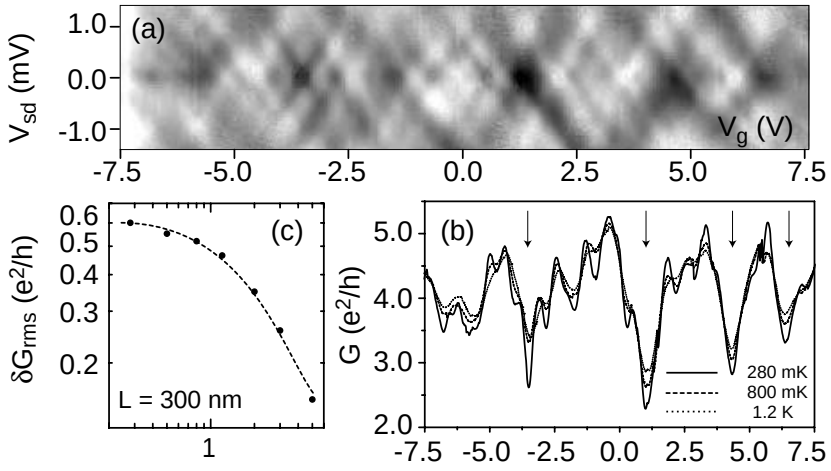

Figure 4.3: **(a)** Grey-scale representation of the differential conductance as a function of source-drain (V_{sd}) and gate voltage (V_g) at 280 mK for an open MWNT device (lighter = more conductive). The separation between the source and drain electrodes is 300 nm. **(b)** Linear-response conductance G as a function of V_g. **(c)** The corresponding root-mean-square δG_{rms} of the conductance fluctuations versus temperature. The saturation of δG_{rms} close to the universal limit suggests conduction through one phase coherent unit.

The conductance variation is interpreted to result from quantum interference. It differs from the patterns observed in nanotube samples with tunnel contacts exhibiting Coulomb blockade (these devices will be discussed in the following chapters). Extended low-conductance regions bounded by high-conductance lines, as expected for Coulomb blockade, are not apparent in the vicinity of $V_{sd} = 0\,\mathrm{mV}$. Instead, well defined conductance dips develop (arrows in Fig. 4.3b). The irregularity of the resonances suggests the presence of scatterers along the tube and should be contrasted to the observation of periodic interference patterns in some ballistic SWNTs [41]. The fact that G often exceeds $4e^2/h$ would be surprising for a SWNT but is consistent with the findings that MWNTs can be substantially hole doped by the environment, allowing more than two spin-degenerate modes to contribute to the current (see chapter 3 or Ref.[42]). For a wire that is 1D with respect to l_ϕ one expects a crossover to the universal value $\delta G_{rms} = 0.73\, e^2/h$ when $l_\phi \sim L$. This appears in the measurement at $T \lesssim 1\,\mathrm{K}$ and δG_{rms} saturates around $0.6\, e^2/h$ at $T_0 = 280\,\mathrm{mK}$, in good agreement with theory [38]. Note that the applied field of 150 mT is not enough to fully destroy time-reversal symmetry in which case $0.52\, e^2/h$ is expected. The saturation of δG_{rms} close to the universal limit suggests con-

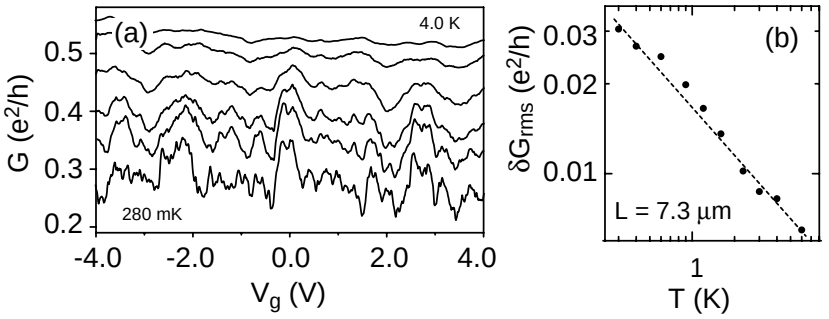

Figure 4.4: **(a)** Linear-response conductance G versus V_g for a 7.3 μm device at temperatures between 280 mK and 4 K. **(b)** The corresponding δG_{rms} versus temperature. The conductance fluctuations are reduced by the series addition of many independent phase coherent units. A best fit of δG_{rms} versus temperature gives a $\propto T^{-0.52}$ dependence.

duction through one phase-coherent unit. This in turn implies that $l_\phi \gtrsim L$ at T_0.

The slope of δG_{rms} versus temperature (plotted on a double logarithmic scale) studied for several short samples varies between -0.3 and -0.8. Deviations from the expected -0.5 exponent might be due to the fact that some samples are (almost) fully phase-coherent, at which point the scaling of Eq. 4.1 should break down. It is also possible that residual electron-electron interaction affects the measurements and is superposed on the interference correction to the conductance. This might explain why the dips in Fig. 4.3 (having the lowest transmission probability) are more pronounced than the peaks. For the longer samples, see e.g. Fig. 4.4, which are far from being fully phase-coherent (expressed in the much lower values of δG_{rms} in Fig. 4.4b as compared to 4.3c) and which have a larger capacitive coupling to the gate electrode (which scales roughly linear with the tube length) a better agreement is obtained.

4.3 Conclusions

The most important conclusions that can be drawn from the interference experiments are that the current in MWNTs flows preferentially in the outermost shell and that the tubes are diffusive (or quasi-ballistic) conductors. The experiments furthermore show that at low temperatures ($T \lesssim 1$ K) the phase-coherence length is of order 1 μm.

Chapter 5

Multiwall nanotubes as quantum dots

In the previous chapter, low-temperature transport measurements on open multiwall carbon nanotube devices have shown that the electron transport can be fully phase-coherent. Here we will present results on a multiwall carbon nanotube device that is more weakly coupled to its leads and for which size and charge quantization of the electron states are of importance. We find that the electron states are nearly fourfold degenerate (including spin) and that their evolution in magnetic field (Zeeman splitting) agrees with a g factor of 2. In zero magnetic field the sequential filling of states evolves with spin S according to $S = 0 \rightarrow 1/2 \rightarrow 0....$ A Kondo enhancement of the conductance is found when the number of electrons on the tube is odd.

5.1 Coulomb blockade and shell filling

While there are many examples of SWNT quantum dots in the literature [43, 44], little effort has gone into the investigation of MWNTs as such systems. Here we will demonstrate that MWNTs can form clean quantum dots as well, a nontrivial result given the larger diameter, the correspondingly smaller energy scale (subband spacing), and, most notably, the diffusive nature of the tubes. Moreover, in MWNT quantum dots the single-particle level spacing δE can exceed the charging energy U_C. This implies that even for a lifetime broadening $\Gamma \sim U_C$ transport occurs via one individual quantum state. Interestingly, the electron levels are found to be nearly fourfold degenerate, a property directly related to the unique band structure of the nanotubes.

Figure 5.1. shows a grey-scale plot of the differential conductance of a $2.3\,\mu$m MWNT device (electrode spacing $L = 300\,$nm) as a function of V_g

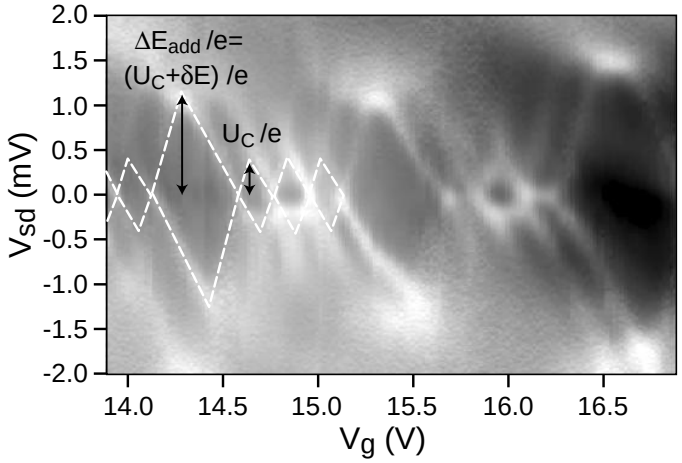

Figure 5.1: Grey-scale representation of the differential conductance as a function of source-drain (V_{sd}) and gate voltage (V_g) at 280 mK (lighter = more conductive). The average two-terminal conductance is high ($\sim 2e^2/h$); nevertheless, clear traces of Coulomb blockade are observed. The pattern of a large diamond followed by three smaller ones suggests a (nearly) fourfold degeneracy (including spin) of the single-electron dot states. ΔE_{add}, U_C, and δE denote the addition energy, the charging energy, and the single-electron level spacing, respectively.

and V_{sd} for relative large positive gate voltages. In the range $V_g \leq 10\,\mathrm{V}$(not shown) the data resembles Fig. 4.3a. In contrast to that device, however, clear and regular traces of Coulomb blockade are visible when V_g is increased beyond $V_g \sim 12\,\mathrm{V}$. These changes are accompanied by a gradually decreasing $\langle G \rangle$ as V_g is increased. The most striking observation in Fig. 5.1 is a sequence of a large low-conduction 'diamond' followed by 3 smaller ones (best seen on the left). The diamonds are highlighted by dashed lines in the figure. The size of the diamonds reflects the magnitude of the addition energy ΔE_{add}, which measures the difference in chemical potential of two adjacent charge states of the dot. In the constant interaction model $\Delta E_{add} = U_C + \delta E$ where $U_C = e^2/C$ is the single-electron charging energy and C the electrostatic capacitance [10]. If all the single-electron levels would repel each other (only 2-fold spin degeneracy) and $\delta E \sim U_C$, an alternating sequence of small and large diamonds would be expected. Starting from an even filling number, $\Delta E_{add} = U_C + \delta E$ for the first added electron (large diamond) and U_C for the second one (small diamond) [45]. The sequence of one large diamond, followed by three smaller ones of approximately equal size, which is observed here, suggests that the degeneracy of the states is not

2, but rather 4 (including spin). From the size of the diamonds we obtain $\delta E \approx 0.8\,\mathrm{meV}$ and $U_C \approx 0.4\,\mathrm{meV}$, the latter corresponding to $C_\Sigma = 400\,\mathrm{aF}$. The total capacitance C_Σ is the sum of the gate capacitance C_g and the contact capacitances C_s (source) and C_d (drain). All three parameters can be deduced from the diamonds. We obtain: $C_g = 1\,\mathrm{aF}$ and $C_{s,d} = 260, 140\,\mathrm{aF}$. An estimate of the lifetime broadening Γ can be obtained from the measured width of the Coulomb peaks and yields $\Gamma \approx 0.25\,\mathrm{meV}$.

The appearance of regularly spaced electron states seems puzzling given the disorder and the substantial hole-doping in MWNTs. To reconcile this we propose transport through a semi-conducting outermost shell and a metallic inner one for this device. The semi-conducting shell will be hole-doped by the environment [42] and conducts at moderate V_g. At large positive gate voltages, however, the tube will be depleted of charge carriers and the 2nd shell (assumed to be metallic) will dominate electron transport, as observed in Ref. [37]. Separated from the dopants on the outside of the MWNT the inner shell then constitutes a clean and largely undoped quantum dot. As the coupling to the leads decays exponentially for inner shells [37] we do not expect more shells to contribute to the current at low temperatures. For the same reason we expect this quantum dot to be extended over the whole nanotube length.

The level spacing δE of an ideal and undoped metallic nanotube is given by $\delta E = hv_F/2L$, where $v_F = 8 \cdot 10^5\,\mathrm{m/s}$ is the Fermi velocity [3]. Assuming L to be the complete tube length of $2.3\,\mu\mathrm{m}$ this yields $\delta E = 0.72\,\mathrm{meV}$ in good agreement with the observed $\delta E \approx 0.8\,\mathrm{meV}$. Transport through a clean and undoped would also explain why the large diamonds of Fig. 5.1 look uniform. This would not be the case if more than the ideally expected 2 modes participate in transport. The appearance of quantized states also shows that transport can be phase coherent over distances of order $1\,\mu\mathrm{m}$, in agreement with the findings for more open devices.

The observation of a ratio $\delta E/U_C > 1$ is particularly interesting. The level spacing δE of an *undoped* tube is independent of diameter and depends only on L. The charging energy, on the other hand, is found to be dominated by the contact capacitances. Given the 10 times larger diameter and overlap with electrodes, MWNTs are more likely to have a small U_C as compared to SWNTs, yielding large $\delta E/U_C$ ratios.

The observed 4-fold degeneracy can be explained by a specific property of graphene. In the simplest tight-binding band-structure calculation all 1D-bands are twofold degenerate (not including spin) [3]. This degeneracy can be traced back to the presence of two C-atoms per unit cell, each contributing with one valence orbital. This so-called $K - K'$-degeneracy has not been observed before, although it is supposed to be a generic feature of graphene. To explore this scenario further we have also studied the

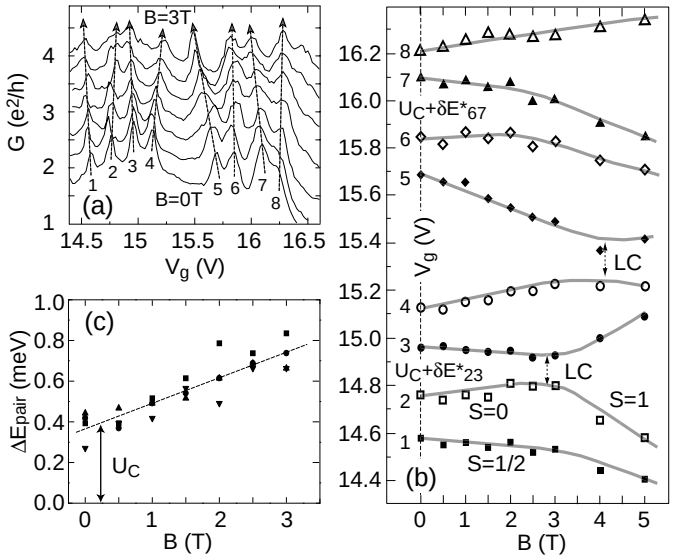

Figure 5.2: **(a)** Linear-response conductance G as a function of gate voltage V_g for different magnetic fields $B = 0 \cdots 3\,\mathrm{T}$ (vertically offset for clarity). The evolution of the conductance peaks are highlighted by dashed lines. **(b)** Peak positions versus $B = 0 \cdots 5\,\mathrm{T}$. Curves are guides to the eye and LC denotes level-crossings. **(c)** Magnetic field dependence of the addition energy deduced from the separation of adjacent peaks involving electrons on the same orbital (the pairs $1 \leftrightarrow 2$ $3 \leftrightarrow 4$, $5 \leftrightarrow 6$, and $7 \leftrightarrow 8$). The dashed line (least-square fit) corresponds to the Zeeman energy with Landé factor $g = 2.1$.

gate-voltage shifts of the linear-response conductance peaks as a function of a magnetic field B perpendicular to the tube axis, Fig. 5.2. The difference between the positions of adjacent peaks can be related to the addition energy: $e\Delta V_g = \Delta E_{add} C_\Sigma / C_g$. Figure 5.2a shows the evolution in small magnetic field $B \leq 3\,\mathrm{T}$. Adjacent peaks are seen to shift in opposite directions. This is the behavior of a ground-state whose spin alternates as $S = 0 \rightarrow 1/2 \rightarrow 0 \cdots$. This indicates that the assumed 4-fold degeneracy is not exact as we will explain now: In the presence of a magnetic field the energy of an electron depends on its spin due to the Zeeman effect which lowers the degeneracy from 4 to 2. When the four (nearly) degenerate states are occupied by $N = 2$ electrons, these are thus expected to occupy different orbitals with *parallel* spins. Actually, this would already be expected for $B = 0$, because of exchange-correlations. Hund's rule would favour the spin-triplet with total angular momentum $S = 1$ when the gain in exchange

energy E_X exceeds the level spacing between single-particle states [46]. The spin should therefore evolve as $S = 1/2 \rightarrow 1$ for $N = 1 \rightarrow 2$. Experimentally, however, the first 2 electrons have opposite spins and are thus added to the same orbital state. This discrepancy can only be resolved, if the assumed 4-fold degeneracy is not exact, i.e. there are pairs of states which lie close together with spacing $\delta E^\star$. The pairs themselves are spaced by $\delta E \gg \delta E^\star$. A detailed study of the peak evolutions (Fig. 5.2b) reveals that this is indeed the case. ΔE_{add} at $B = 0$ of the $2 \rightarrow 3$ ($6 \rightarrow 7$) transition is clearly larger than the $1 \rightarrow 2$ and $3 \rightarrow 4$ ($5 \rightarrow 6$ and $7 \rightarrow 8$) ones. We obtain $\delta E^\star_{23} \approx 0.1\,\mathrm{meV}$ and $\delta E^\star_{67} \approx 0.18\,\mathrm{meV}$. We have also verified that the energy shifts agree with the Zeeman term for electrons occupying the same orbital. We plot in Fig. 5.2c the corresponding addition energies as a function of B. A best fit of the data to $U_C + g\mu_B B$, where μ_B is the Bohr magneton and g the Landé factor, is shown as a dashed line and yields $g = 2.1 \pm 0.3$. This value is consistent with $g = 2.0$ for graphite and with previous measurements of g for a SWNT [43, 47].

In high magnetic field levels cross. Two crossings (LCs) are seen in Fig. 5.2b. At $B \approx 3\,\mathrm{T}$, for example, the spin-up of the first orbital crosses the spin-down of the second, giving rise to an $S = 0 \rightarrow 1$ transition. A similar crossing is not seen in the upper part. On the one hand, this is due to the larger $\delta E^\star$. On the other hand, there is also a magnetic-field dependence of the orbitals which increases $\delta E^\star$ at higher fields.

We find a pattern that repeats every 4th electron due to an apparent *pairing* of orbital states. We believe that this pairing is related to the $K-K'$-degeneracy. Hybridization via the contacts is proposed as a possible mechanism for the slight level splitting $\delta E^\star$ of the orbital states, which in size is comparable to the life-time broadening. Alternatively, scatterers which lower the symmetry of the system may cause the level splitting. In high magnetic field the intrinsic $K - K'$-degeneracy should be lifted which enhances the level separation further. This may explain why the $S = 0 \rightarrow 1$ transition is not observed for the upper quartet in Fig. 5.2b. Finally, the fact that $S = 0$ for $N = 2$ at $B = 0$ is consistent with Hund's rule only if the exchange energy $E_X < \delta E^\star$, yielding an upper bound for E_X of $\sim 0.1\,\mathrm{meV}$.

5.2 Kondo physics in multiwall nanotubes

Another interesting manifestation of the electron spin on the electronic transport can be seen in the gate region between 15.5 and 16.5 V, see Fig. 5.3. In the valleys marked as E (even filling) the conduction decreases with decreasing temperature while it increases in the valleys marked as O (odd filling). Contrary to what one might expect from normal CB, a high

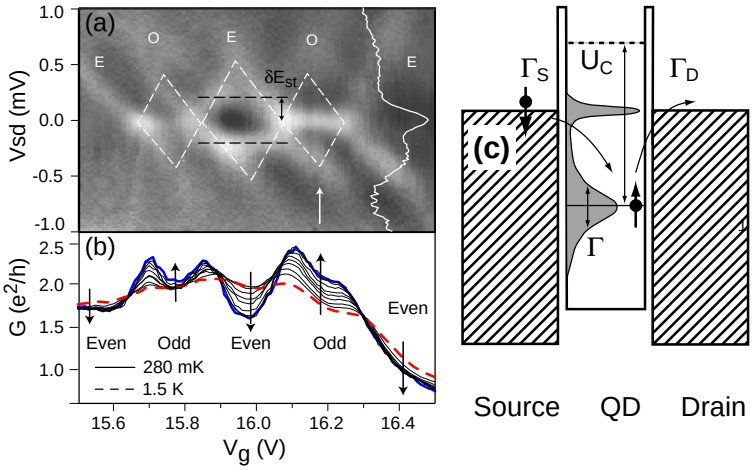

Figure 5.3: **(a)** Grey-scale representation of dI/dV as a function of source-drain (V_{sd}) and gate voltage (V_g) at 280 mK (lighter = more conductive). Within regions marked as O (E) the number of electrons on the tube is odd (even). The horizontal features are caused by the Kondo effect. **(b)** Temperature dependence of the linear-response conductance. The arrows indicate directions of decreasing temperature. **(c)** Schematics of a quantum dot in the Kondo regime. The dot is occupied by an odd number of electrons. Driven by exchange correlation effects between the dot state and the electrons in the leads, higher-order spin-flip processes screen the spin of the dot and form a resonance in the DOS at the Fermi energy of the leads.

conduction 'ridge' around $V_{sd} = 0\,\mathrm{V}$ develops in the latter (best seen in the right most diamond). These observations can be understood with the Kondo model [48, 49]. When the number of electrons on the tube is odd and the coupling to the leads is strong enough to allow for higher-order tunneling processes, a spin singlet can form between the spin polarized tube and electrons in the leads. This results in a resonance in the density-of-states at the Fermi energy (i.e. the Kondo resonance). The width of the Kondo resonance reflects the binding energy of the singlet which is usually described by a Kondo temperature T_K. The conductance is expected to increase logarithmically with decreasing temperature in the centers of the ridges below T_K. Following G as a function of temperature at $V_g = 16.2\,\mathrm{V}$ we indeed find a logarithmic dependence between 280 mK and 1 K. At temperatures well below T_K the conductance is expected to saturate at the unitary limit of $2e^2/h$. In our case, however, no saturation has been observed down to 280 mK.

The Kondo effect is expected to be suppressed by a small bias voltage across the tube of the order of $\pm k_B T_K/e$. The ridge at $V_g = 16.2$ V has a width of ~ 0.2 meV which would correspond to $T_K = 1.2$ K (see curve in Fig. 5.3a). This is in agreement with the onset of the logarithmic increase of G below ~ 1 K. An additional prediction is the splitting and disappearance of the Kondo resonance in a magnetic field. The high-conductance ridge indeed broadens and disappears above ~ 1.5 T. Simultaneously, the Coulomb blockade diamonds are recovered. Measurements on a different device in which the splitting in field could be more clearly resolved are shown in App. C. In Fig. 5.3a the boundary of the CB region at half-filling is clearly seen to be distorted into a truncated diamond. The associated energy $\delta E_{st} = 0.20 \pm 0.05$ meV, indicated in the figure, corresponds to the energy difference between the singlet ground state and the triplet excited state [49, 50]. The relation $\delta E_{st} = \delta E^{\star}_{67} - E_X$ together with $\delta E^{\star}_{67} \sim 0.18$ meV shows that E_X must indeed be small.

In conclusion, we show that MWNTs can form clean quantum dots in which the level separation exceeds the charging energy. Moreover, we observe a pairing of 0D states which we propose to be caused by the $K - K'$ degeneracy generic to graphene. Since adsorbates on the outside of a NT are a likely source of scattering, the ability to selectively address clean inner shells of a MWNT may prove advantageous in this regard.

Chapter 6

Suppression of tunneling into multiwall nanotubes

Carbon nanotubes (NTs) are emerging as an excellent system for the investigation of electronic transport in one dimension (1D). Two different classes of NTs exist: small diameter ($\approx$1 nm) single-wall NTs (SWNTs) and large diameter ($\approx$ 10nm) multi-wall NTs (MWNTs). Metallic SWNTs are characterized by two 1D channels and long mean free paths: $l > 1\,\mu$m [43, 44, 51, 52]. As such, they represent a nearly perfect 1D system. It is well known that in 1D transport is strongly affected by electron-electron (e-e) interaction, producing a system called a Luttinger-liquid (LL) whose low energy states are collective in nature [53, 54]. The tunneling density of states (tunneling DOS = TDOS) of a LL diminishes as a power law with energy according to $\nu \propto E^{\alpha}$ with different exponents α for different geometries, e.g. whether the electron tunnels into the end or the bulk. The tunneling conductance $G \propto$ TDOS has been measured for SWNTs in a variety of geometries and good agreement with LL predictions have been achieved [55, 56, 57].

Various experiments on the transport properties of MWNTs have been performed. Experiments with low resistance contacts show interference effects, such as Aharonov-Bohm oscillations [31, 32], weak localization, and universal conductance fluctuations [31, 58]. These have been used to infer the mean free path, yielding $l \lesssim 100\,$nm. They also indicate that the dc current is predominantly carried in the outer shell of the NT. Similarly, transport [31] and scanned probe experiments[52, 59] indicate a typical resistance per unit length of $5 - 10\,\mathrm{k}\Omega/\mu$m.

Here we discuss measurements of the tunneling conductance of MWNTs. In one geometry, metallic contacts to the tube with high resistance are employed. In a second geometry, NT-NT junctions are created by manipulation with an atomic force microscope (AFM). The tunneling conductance is mea-

sured as a function of temperature and bias voltage. These measurements show that also for MWNTs the TDOS is a power law over a wide energy range of $1 \lesssim E \lesssim 100\,\mathrm{meV}$ with geometry-dependent exponents, which surprisingly agree quite well with those for SWNTs. This suggests a similar origin. Unlike SWNTs, however, MWNTs are diffusive or at best quasi-ballistic, so that the applicability of LL theory must be carefully considered.

Power laws in tunneling may also be caused by the disorder-enhanced Coulomb interaction, as was treated perturbatively in the seminal work of Altshuler, Aronov and Lee (AAL) [60]. Importantly, perturbation theory does not suffice for MWNTs since the observed corrections are large. A non-perturbative treatment, applied to the specific geometry of MWNTs, has recently been put forward by Egger and Gogolin (EG) [61]. Similar to LL theory, a power-law is predicted. We will therefore compare our measurement with both the EG and the LL model.

The MWNTs were synthesized by arc-discharge evaporation and deposited from a dispersion in chloroform onto an oxidized Si wafer. NTs with diameters ranging from 8 to 17 nm are selected and located using a scanning electron microscope or an AFM. For devices of the first type, gold contacts to the tube are then created using e-beam lithography. This procedure typically leads to contacts with low resistance ($\approx 1\,\mathrm{k}\Omega$), but it also occasionally produces highly resistive contacts ($>10\mathrm{k}\Omega$). The microscopic origin of the high resistance is not known. Here, however, we merely exploit these accidental tunnel barriers to probe the electronic properties of the MWNT.

The inset of Fig. 6.1 shows a schematic of a device consisting of a $d = 17\,\mathrm{nm}$ diameter MWNT contacted to 3 electrodes. The $4.5\,\mathrm{k}\Omega$ resistance measured between the two outer electrodes corresponds to the typical intrinsic resistance for a MWNT contacted with electrodes that are separated by 700 nm. This indicates that the contact resistances of the two outer electrodes are low and that the NT connecting them is electrically continuous. However, the resistance measured from the inner electrode to either of the outer electrodes is much higher, $140\,\mathrm{k}\Omega$. This inner electrode has thus low transparency and serves as a tunneling contact to explore the TDOS of the tube.

Fig. 6.1 shows a series of measurements of the tunneling conductance versus bias for different magnetic fields B applied parallel to the tube. The dI/dV spectra are highly structured. We first note that, at small energies ($0 - 10\,\mathrm{mV}$) the spectra display a strongly suppressed conductance. This suppression is centered at $V = 0$ independent of B. Before discussing this anomaly, we first will briefly address the complex features at higher energy. These features are quasi-periodic, with an average spacing between the maxima of $\approx 25\,\mathrm{mV}$ and they evolve with increasing magnetic field.

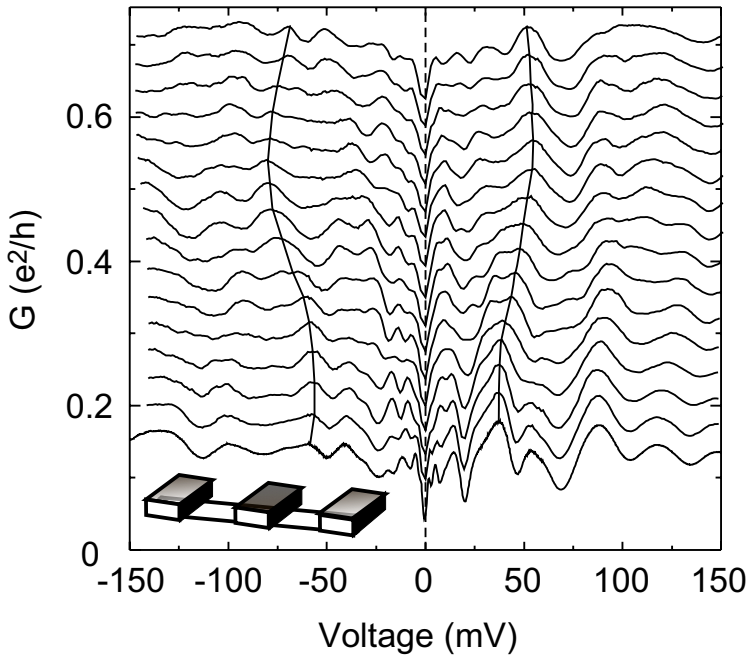

Figure 6.1: $G = dI/dV$ as a function of V at 2 K for different parallel magnetic fields $B = 0, 1, \ldots 15$ T. Curves are offset for clarity. The movement with B of two well discernable peaks are indicated by solid curves. Inset: schematic of MWNT-Au devices with 3 electrodes, here separated by 350 nm. The inner electrode has a high resistance and serves as tunneling contact for measuring dI/dV.

The observed features are likely a consequence of quasi 1-dimensionality. One-dimensional states (so called 1D-subbands) have a pronounced energy-dependent DOS with peaks at the subband threshold (van Hove singularity) [18, 27]. Here, the peaks are broadened due to scattering from disorder. This assignment is supported by the observed peak spacing of ≈ 25 meV which is in good agreement with the expected spacing of $\hbar v_F/d = 29$ meV ($v_F = 8\ 10^5$ m/s is the Fermi velocity, $d = 17$ nm). The identification of these peaks as broadened van Hove peaks is further supported by their behavior in B. With evolving parallel field B the position of the peaks move in energy up and down, as expected from the Aharonov-Bohm effect [62]. Theory predicts a periodic movement with a fundamental period h/e which translates into a field of ≈ 17 T. Though the level moves on the expected field scale, the peak movement is not simple in Fig. 6.1. The reason is not clear yet, but may be attributed to disorder and inhomogeneities. The

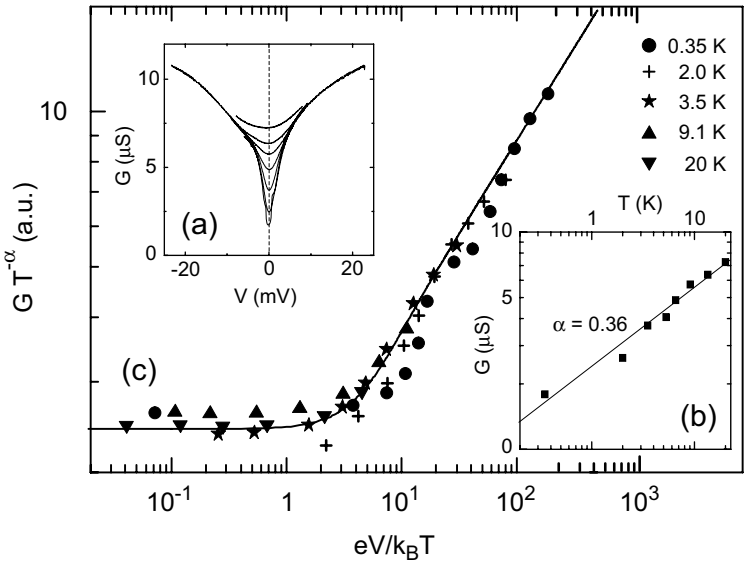

Figure 6.2: **(a)** $G(V, T = \text{const}) = dI/dV$ of a 2nd MWNT for $T = 0.35 \ldots 20\,\text{K}$. **(b)** The linear conductance $G(0, T)$ in a double logarithmic plot demonstrating power-law scaling. **(c)** $G(V, T) \cdot T^{-\alpha}$ versus eV/k_BT. Similar to the T dependence, $G \propto V^\alpha$ for $eV \gg k_BT$ with power $\alpha = 0.36$.

emergence of *broadened* van Hove peaks in the TDOS demonstrates that the elastic length l is of the same order as the circumference of the tube. The MWNTs are therefore not in the two-dimensional diffusive regime ($l < d$).

We now turn to the low bias suppression of the conductance. It is independent of B, which suggests a different origin than the peaks discussed above. In addition, its dependence on V and T is very different, as we now discuss. Fig. 6.2 shows the tunneling conductance $G = dI/dV$ of a second, similarly prepared MWNT sample. A conductance dip centered at zero bias (zero-bias anomaly = ZBA) is again observed in $G(V)$ (Fig. 6.2a). As T is decreased down to 350 mK, the amplitude of the dip increases. In Fig. 6.2b the zero bias conductance is plotted as a function of T in a double logarithmic plot, demonstrating that the measured data can be well described by a power law $G \propto T^\alpha$ with exponent $\alpha = 0.36$. For bias voltages larger than k_BT/e, the voltage dependence can also be described by a power law with the same exponent 0.36. This can be seen in Fig. 6.2c, which shows a double-logarithmic plot of the symmetrical part of G divided by T^α as a function of eV/k_BT. All data collapse on a single universal curve, similar to what has been observed in SWNTs [55]. Power-law scaling in T and V

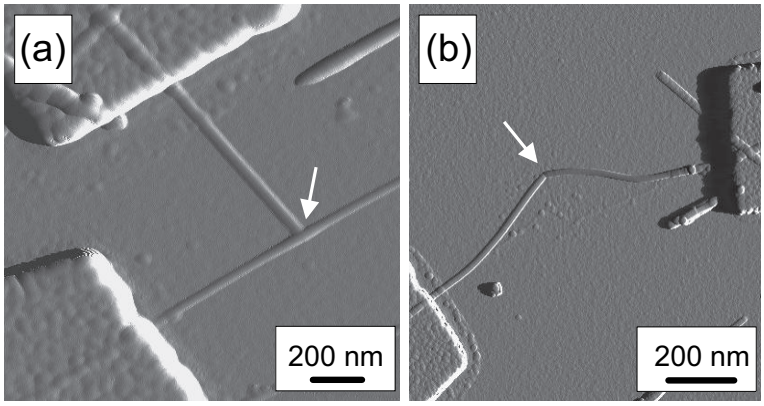

Figure 6.3: AFM images of junctions formed between two MWNTs: **(a)** end-bulk junction, and **(b)** end-end junction. The arrows indicate the position of the junctions.

has been found in 11 different samples with exponents α ranging from 0.24 to 0.37.

To explore this ZBA further, we created devices composed of 2 MWNTs arranged in different geometries. An AFM tip has been used to move NTs [57, 63]. The end of one tube is pushed against either the end or the middle (bulk) of a second tube. Au contacts are attached to both tubes. Examples of end-bulk and end-end junctions are shown in Fig. 6.3a and 6.3b, respectively. The resistance values of these junctions vary considerably, from immeasurably large to $\approx 100\,\mathrm{k}\Omega$. These large values suggest that the junction between two tubes serves as a tunnel barrier.

As in metal-NT junctions, pronounced ZBAs are present in all junctions. However, the suppression is significantly more dramatic in NT-NT as compared to Au-NT junctions. Fig. 6.4a shows dI/dV as a function of V in a double logarithmic scale at $T = 3\mathrm{K}$ for a bulk-end and an end-end junction. For comparison, the tunneling conductance of a typical Au-NT junction is also plotted. The curves show approximate power law behavior, but with different exponents. We find $\alpha = 0.9$ and 1.24 for bulk-end and end-end NT-NT junctions. These exponents are representative of seven junctions studied.

Overall, our result for tunneling into MWNTs can be summarized by a simple rule. The conductance is given by $G \sim E^{\alpha}$, where E is the excess energy of the tunneling electron, given by the larger of eV or k_BT. The exponent α can be approximated by $\alpha = \alpha_1 + \alpha_2$, where $\alpha_{1,2}$ represent the

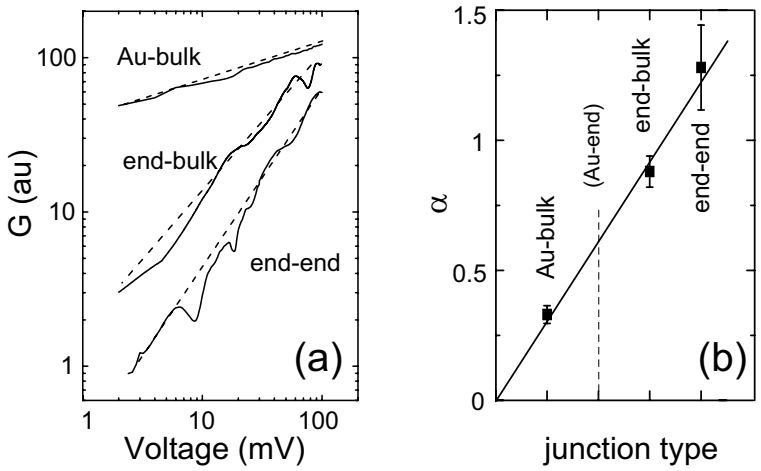

Figure 6.4: **(a)** G as a function of V in a double logarithmic plot for a Au-bulk, an end-bulk and an end-end junction. The corresponding slopes are $\alpha = 0.25$, 0.9 and 1.24, respectively. **(b)** plot of α as a function of the junction type for Au-Au, Au-bulk, Au-end, bulk-end, and end-end junctions.

properties of the conductor on either side of the junction: $\alpha^{bulk} \sim 0.3$ for the tube bulk, $\alpha^{end} \sim 2\alpha^{bulk} \sim 0.6$ for the tube end, and $\alpha \sim 0$ for the Au contact, respectively.

We now discuss the possible origins of the ZBA. The voltage and temperature dependence of G could be caused by the energy dependence of the single particle DOS of graphene, the 2D material from which NTs are made. The 2D-DOS of graphene is $\propto E$, which would relate into $\alpha^{bulk} = 1$, in contradiction to the observation. Moreover, if the observed anomaly would be related to the single particle DOS, its position would depend on gate voltage (back gate), which is not observed.

A ZBA in the TDOS is often taken to be a signature of e-e interactions. For example, the correction (suppression) to the density of states ν due to e-e interaction has been calculated by AAL perturbatively, valid if $\delta\nu \ll \nu$, or $\delta G \ll G$ [60]. This interpretation has been successful in describing ZBAs in tunnel contacts to disordered metals [64]. In contrast to these earlier experiments, we report on anomalies with large amplitudes $\delta G \sim G$. A quantitative understanding requires to calculate the TDOS nonperturbatively in the interaction.

Nonperturbative treatments exist for a number of cases. In the case of a clean 1D quantum wire, the e-e interaction can be accounted for analytically at any strength leading to a Luttinger liquid (LL),[53]. The case of a tunnel

junction whose coupling to the ideal reservoirs is described by a frequency dependent impedance $Z(\omega)$ has also been studied extensively [65]; we refer to this as the environmental Coulomb blockade theory (ECBT). The LL and ECBT theories bare a lot in common. Tunneling into a LL excites plasmon modes which can be understood as the eigenmodes of an LC-transmission line, where L is the kinetic inductance and C the external electrostatic capacitance. The impedance Z of such an ideal transmission line is ohmic with $Z = R = \sqrt{L'/C'}$, where L' and C' denote inductance and capacitance per unit length. In the limit of many modes in parallel, both theories give $G \propto V^{\alpha}$ (at $T = 0$) with $\alpha^{end} = 2R/R_K$, where $R_K = h/e^2$ is the quantum resistance [66, 67].

These theories also predict $\alpha^{end}/\alpha^{bulk} = 2$ for a large number of modes. The factor 2 reflects the fact that a quasiparticle added to the bulk can propagate away into the 'right' and 'left' arm of the NT, while it can propagate only in one arm if added to the end. In the spirit of ECBT the effective environmental impedance is halved. This can be generalized to other geometries. In terms of α^{bulk}, both theories predict $\alpha^{end} = 2 \cdot \alpha^{bulk}$, $\alpha^{bulk-end} = 3 \cdot \alpha^{bulk}$, and $\alpha^{end-end} = 4 \cdot \alpha^{bulk}$.

The limit of many modes applies to our experiment, since MWNTs have recently been shown to be considerably hole doped [42]. Due to doping $N \approx 10 - 20$ subbands are occupied, instead of 4 for an ideal SWNT. The large-N LL/EBCT theory should therefore apply. Indeed the data is in very good agreement with the predictions. The power-law exponents increase as predicted with changes in geometry; see Fig. 6.4b (solid line). We can also numerically estimate the exponent. The kinetic inductance is given by $L' = R_K/2Nv_F$, where $v_F \approx 10^6\,\mathrm{m/s}$ is the Fermi velocity and $N \approx 10 - 20$ the number of modes, yielding $L' \approx 1\,\mathrm{nH}/\mu\mathrm{m}$. A typical value for the (external) capacitance of a nanotube is $C' = 30\,\mathrm{aF}/\mu\mathrm{m}$. These values yield a transmission line impedance of $R \approx 5.7\,\mathrm{k}\Omega$, and consequently a bulk exponent of $\alpha^{bulk} \approx 0.22$, a value which is in reasonable agreement with the measured exponents. It therefore appears that ECBT assuming a fixed-impedance environment (such as an LC transmission line), or equally, the LL theory in the large N limit, explain our observations.

So far, however, we ignored that the MWNTs are disordered conductors. Because MWNTs are disordered, it is more appropriate to model the NT as an RCL transmission line rather than an LC one. Let us estimate the significance of the resistance. We compare $\omega L'$ with $R' \approx 5\,\mathrm{k}\Omega/\mu\mathrm{m}$. The inductive part is equal to the resistive part for $\hbar\omega = 3.0\,\mathrm{meV}$. Since the power-law is observed for larger voltages, the resistive part can in fact be neglected. Therefore, the LC transmission line model is applicable for not too small voltages.

We now compare our data with a nonperurbative treatment of the dis-

order enhanced renormalization of the TDOS caused by intra-Coulomb interaction. This topic has only recently become the subject of intensive theoretical studies [61, 68, 69]. For MWNTs this problem has been solved by Egger and Gogolin [61]. They predict a power-law with exponent $\alpha^{end} = 2\alpha^{bulk} = (r/\pi D\hbar\nu_0)\log(1+\nu_0 U_0)$, where U_0 is the 1D intra-Coulomb interaction, r the radius of the tube, and D the diffusion constant. The log() term turns out to be $\sim 2-3$ and the (bare) DOS is $\nu_0 = N^\star/2\pi\hbar v_F$. Here, $N^\star$ denotes the number of modes not counting the spin and K-K' degeneracy of the graphene lattice, i.e. $N^\star = N/4 \approx 5$. This yields $\alpha^{bulk} \approx 5r/N^\star l_e = 20r/Nl_e$. This equation can be expressed solely in terms of measured quantities by noting that $R' = R_K/Nl_e$, yielding $\alpha^{bulk} \approx 20rR'/R_K = 0.02\ldots0.08$. The typical value is roughly a factor 5 smaller than observed in the experiment. As a result, the large-N LL/EBCT model is the more likely cause of the observed suppression of tunneling.

In conclusion, the tunneling DOS of MWNTs is renormalized by e-e interaction leading to a suppression of the tunneling conductance for small energies with power-law scaling. The observed power-laws can be explained by environmental Coulomb blockade theory in which the tube acts as an effective LC-transmission line in series with the tunnel junction. The observed power-laws are qualitatively also captured by a recent nonperturbative treatment of disorder-enhanced corrections to the DOS due to intra-Coulomb interaction. The comparison of the measured exponents with theoretical predictions favors the LC transmission line model. Further experimental work is needed to separate these two contributions.

Chapter 7

Superconducting proximity effect in multiwall nanotubes

In this chapter electron transport in MWNTs coupled to superconducting electrodes is investigated. We have studied MWNT devices with strong, intermediate, and weak coupling to superconducting leads. In the weak coupling limit (not shown here) electron transport is dominated by Coulomb blockade. In the intermediate regime on the other hand, higher order tunneling processes such as the Kondo effect become important. In section 7.2 we discuss a MWNT quantum dot in the Kondo regime coupled to superconducting electrodes. We show that the superconductivity of the leads does not destroy the Kondo correlations on the quantum dot when the Kondo temperature, which varies for different single-electron states, exceeds the superconducting gap energy. The observed subharmonic gap structure in the differential conductance is discussed in section 7.3 and compared to a theoretical model of the device. The transport characteristics of an open MWNT device are discussed below.

7.1 Open multiwall nanotube devices

Transport measurements of an open MWNT device with superconducting electrodes are shown in Fig. 7.1. The device consists of a MWNT of 2.2 μm length with short ($L = 300$ nm) contact spacing. The contacts consist of a bilayer of Au/Al of 50/125 nm thickness respectively. The degenerately doped Si substrate is used as a gate electrode. This geometry is typical for all devices with Au/Al leads studied. The gold is in direct contact to the MWNT and is necessary to obtain good electrical contact between the tube and the leads. As will be shown below, the aluminum becomes superconducting at $T \lesssim 1\,\mathrm{K}$. Due to the proximity of the aluminum, the

gold develops a gap of $2\Delta \approx 0.15\,\mathrm{meV}$ at the interface with the MWNT (see Fig.7.1c). This value is smaller than the expected bulk value for Al which is 0.38 meV. This is attributed to the intermediate Au layer. Indeed we find that for smaller Au layers the gap size is increased. Similar findings have been reported for measurements on break junctions consisting of an Au/Al bilayer [70]. Evaporation of aluminum directly over the MWNTs resulted in immeasurably large contact resistances, probably because an oxide layer forms at the interface between the MWNT and aluminum. This has been exploited in section 3.2 to make local Al gates.

Normal-state conductance

Figure 7.1a shows a grey-scale representation of the differential conductance versus V_{sd} and V_g at $T = 280\,\mathrm{mK}$ when the contacts are driven normal by a small magnetic field of 150 mT (which is much larger larger than the experimentally observed critical field of $\sim 12\,\mathrm{mT}$). The corresponding linear-response conductance G is shown in Fig. 7.1b. Large and reproducible fluctuations of order e^2/h develop in G versus V_g. The average conductance is quite large, $\langle G \rangle \sim 4\ \mathrm{e}^2/\mathrm{h}$. The conductance variation is interpreted to result from quantum interference (UCF). It differs from patterns observed in nanotube samples with tunnel contacts, exhibiting Coulomb blockade. The pattern is not periodic and extended low-conductance regions bounded by high-conductance lines, as expected for Coulomb blockade, are not apparent in the vicinity of $V_{sd} = 0$ V. The fact that G often exceeds $4\,e^2/h$ implies that more than the ideally expected two spin-degenerate modes contribute to the current (see also section 4.2).

Superconducting-state conductance

Figures 7.1c-g show the (differential) conductance of the same device when the leads are superconducting, i.e. when the magnetic field is switched off. The most striking difference between Figs. 7.1a and 7.1c are the high-conductance bands at $V_{sd} = \pm\ 0.15$ mV, almost independent of V_g. These lines are identified as 2Δ and mark the onset of direct quasi-particle tunnelling between source and drain electrode.

The (differential) conductance at $V_{sd} < 2\Delta$ varies significantly with the gate voltage. It is assumed that the main effect of changing V_g is to change the Fermi energy of the nanotube. This changes the transmission probabilities of the different modes connecting the source and drain electrodes. As a results, the conductance versus V_g fluctuates randomly (but reproducible) by $\sim e^2/h$ when the device is in the normal state, as observed in Fig. 7.1b.

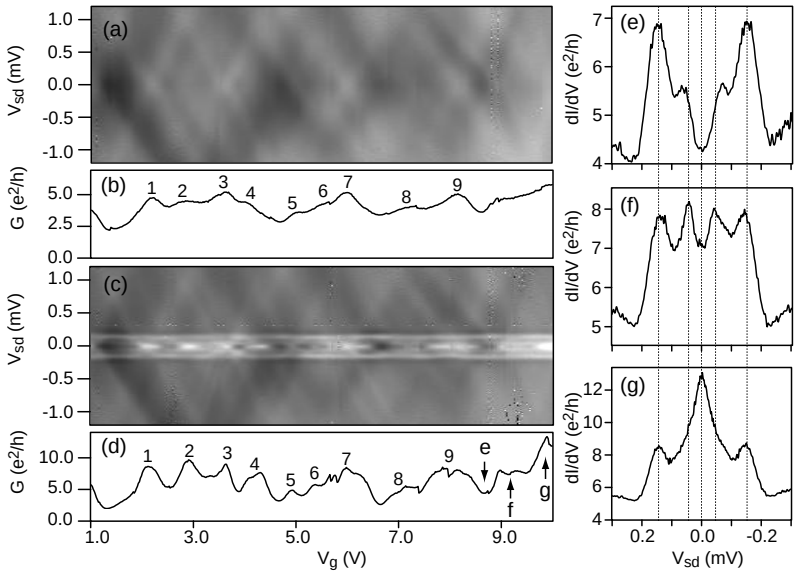

Figure 7.1: **(a)** Grey-scale representation of the differential conductance as a function of source-drain (V_{sd}) and gate voltage (V_g) at $T = 280\,\mathrm{mK}$ for an open MWNT device in the normal state (lighter = more conductive). A small field of 150 mT has been applied. The conductance variation is interpreted to result from quantum interference (UCF). **(b)** Corresponding linear-response conductance. The numbers indicate peaks in the conductance. **(c)** Differential conductance versus V_{sd} and V_g when the leads are superconducting. The bands at ± 0.15 mV mark the onset of direct quasi-particle tunnelling. The subgap structure is due to (multiple) Andreev reflection. **(d)** Corresponding linear-response conductance. The numbered peaks of panel (b) appear enhanced in the superconducting state. **(e-g)** Differential conductance at the positions given in panel (d).

As the conduction is more sensitive to the transmission probabilities when the leads are superconducting, one might expect small differences in G to be enhanced in the superconducting state as compared to the normal state. Indeed, the features (conductance differences between valleys and peaks) in the linear-response conductance of Fig. 7.1b are much clearer in Fig. 7.1d.

The variation in transmission probabilities is also expressed in the differential conductance. Figure 7.1e-g shows dI/dV versus V_{sd} at 3 different positions of V_g, having different normal state conductances (G increases going from position e to g). Although the total conductance is never small, a clear gap appears in Fig. 7.1e, around $V_{sd} = 0$ meV, followed by peaks at Δ and 2Δ. In contrast, a large peak at $V_{sd} = 0$ meV shows up in Fig. 7.1g

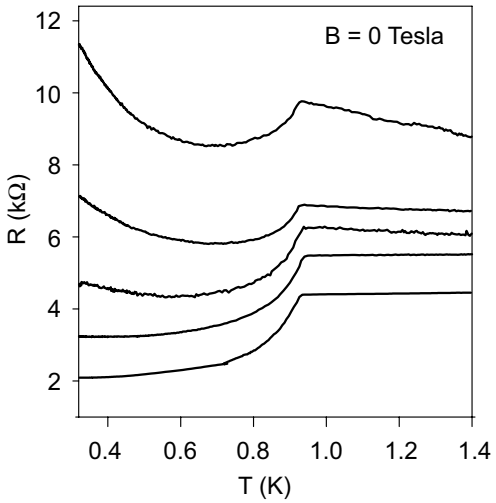

Figure 7.2: Resistance as a function of temperature of an open MWNT device between Au/Al electrodes for 5 different gate positions. A clear transition occurs around $T = 950$ mK.

having a linear-response conductance of more than 12 e^2/h. These are all clear indications that we have indeed observed (multiple) Andreev reflection in our MWNT devices [71].

The temperature dependence for this device at 5 different V_g with increasing resistance is shown in Fig. 7.2. A clear transition is observed around $T = 950$ mK for all traces. Although Fig. 7.2 suggests a clear one-to-one relation between the normal and superconducting state resistances, this is only a trend and 'crossing' $R(T)$ lines have also been observed.

7.2 A quantum dot in the Kondo regime

The electron spin is of central importance in two of the most widely studied many-body phenomena in solid-state physics: the Kondo effect and superconductivity. The Kondo effect can be understood as a magnetic exchange interaction between a localized impurity spin and free conduction electrons [48]. In order to minimize the exchange energy, the conduction electrons tend to screen the spin of the magnetic impurity and the ensemble forms a spin singlet. In an s-wave superconductor the electrons form pairs with antialigned spins and are in a singlet state as well. When present simultaneously, the Kondo effect and superconductivity are usually expected to

be competing physical phenomena. In a standard s-wave superconductor containing magnetic impurities, for example, the local magnetic moments tend to align the spins of the electron pairs in the superconductor which often results in a strongly reduced transition temperature. A more subtle interplay has been proposed for exotic and less well understood materials such as heavy-fermion superconductors in which both effects might actually coexist [72].

Given the complexity of a system involving two different many-body phenomena, it would be highly desirable to have a means to investigate their mutual interplay at the level of a single impurity spin. In this respect, the study of a quantum dot as an artificial impurity in between superconducting reservoirs is of great interest. This approach has already proved very successful in the study of the Kondo effect in normal metals [73, 74, 49]. Here we achieve this for a carbon nanotube quantum dot coupled to superconducting Au/Al leads.

The device we consider consists of an individual MWNT of 1.5 μm length between source and drain electrodes that are separated by 250 nm [75]. The lithographically defined leads were evaporated over the MWNT, 45 nm of Au followed by 135 nm of Al. The degenerately doped Si substrate was used as a gate electrode. Low-temperature transport measurements of the device exhibited pronounced superconducting proximity effects, as did all other 14 measured samples having Au/Al contacts.

Before investigating the influence of the superconducting correlations in the leads, the sample is characterized with the contacts driven normal by a magnetic field of 26 mT. This field is quite small in terms of the Zeeman energy ($g\mu_B B = 3.0\,\mu$eV at $B = 26\,$mT where μ_B is the Bohr magneton and $g \simeq 2$ the gyromagnetic ratio) but exceeds the critical field of the electrodes, which was experimentally determined to be $\sim 12\,$mT, see App. C. Figure 7.3 shows a grey-scale representation of the differential conductance as a function of source-drain (V_{sd}) and gate voltage (V_g). An alternating sequence of truncated low-conduction 'diamonds', linked by narrow ridges of high conduction can be seen. The size of the diamonds reflects the magnitude of the addition energy ΔE_{add} which measures the difference in chemical potential of two adjacent charge states of the dot. In the constant interaction model $\Delta E_{add} = U_C + \delta E$, where $U_C = e^2/C_\Sigma$ is the single-electron charging energy, C_Σ the total electrostatic capacitance and δE the single-electron level spacing [10]. Starting from an even filling number, $\Delta E_{add} = U_C + \delta E$ for the first added electron (large diamond) and U_C for the second one (small diamond). The horizontal features at $V_{sd} \neq 0\,$mV truncating the large diamonds are attributed to the onset of inelastic co-tunneling. From the size of the truncated diamonds we obtain $\delta E \approx 0.40 - 0.70\,$meV. The charging energy is obtained from the size of the (faintly visible) small diamonds and

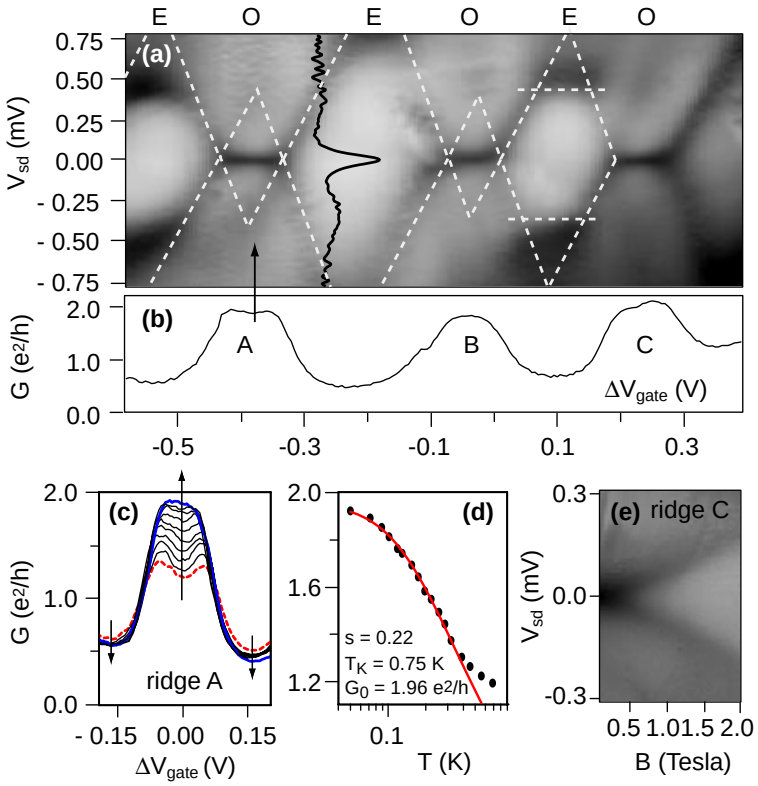

Figure 7.3: **(a)** Grey-scale representation of the differential conductance as a function of source-drain (V_{sd}) and gate voltage (V_g) at $T = 50\,\mathrm{mK}$ and $B = 26\,\mathrm{mT}$ for a MWNT device in the Kondo regime (darker = more conductive). The dashed white lines outline the Coulomb diamonds. The black curve shows the dI/dV_{sd} versus V_{sd} trace at the position of the arrow. The regions with even and odd number of electrons are labelled E and O, respectively. **(b)** Linear-response conductance G as a function of V_g. The Kondo ridges are labelled A, B and C. **(c-d)** Temperature dependence of ridge A between 50 mK (thicker line) and 700 mK (dashed line). The data can be fitted using the empirical function given in the text yielding a Kondo temperature for ridge A of $\sim 0.75\,\mathrm{K}$. **(e)** When a magnetic field is applied ($0.1 - 2\,\mathrm{T}$), the ridges split into components at $V_{sd} = \pm g\mu_B B/e$.

yields $U_C \approx 0.45\,\mathrm{meV}$.

The high-conductance ridges are a manifestation of the Kondo effect occurring when the number of electrons on the dot is odd (total spin $S = 1/2$). The width of the Kondo resonance reflects the binding energy of the spin singlet between the spin polarized dot and the electrons in the leads and is usually described by a Kondo temperature T_K. Several of the Kondo ridges observed show a conductance saturation at the lowest temperatures and the valley between peaks has completely disappeared at $T \approx 50\,\mathrm{mK}$, which is the base electron temperature of our dilution refrigerator. Figures 7.3c-e show that the Kondo ridges follow the expected behavior such as a logarithmic increase of the linear-response conductance G below T_K, a saturation of G at $T \ll T_K$ and a linear splitting into components at $V_{sd} = \pm g\mu_B B/e$ when a magnetic field is applied.

From the width of the Kondo ridge out-of-equilibrium, the full width at half-maximum (FWHM) corresponds to $\sim k_B T_K$, we estimate a Kondo temperature of 0.82 K for ridge 'A' [76]. The Kondo temperature can also be obtained from the temperature dependence of the linear-response conductance. In the middle of the ridge this is given by the empirical function: $G(T) = G_0/(1 + (2^{1/s} - 1)(T/T_K)^2)^s$, where $s = 0.22$ for a spin 1/2 system and G_0 is the maximum conductance [77]. A best fit to the data yields $G_0 = 1.96\,e^2/h$ and $T_K = 0.75\,\mathrm{K}$, in agreement with the estimate of T_K from the width of the Kondo ridge. From here on the width of the resonance out-of-equilibrium is taken as the measure of T_K. For the ridges 'B' and 'C' this yields T_K's of 1.11 K and 0.96 K respectively.

We now turn to the behavior of the conductance when the magnetic field is switched off and the reservoirs become superconducting. Figure 7.4 shows a grey-scale representation of the differential conductance versus V_{sd} and V_g for the same gate range of Fig. 7.3 at $B = 0\,\mathrm{mT}$. Note that the vertical axis is shown only between -0.3 and 0.3 mV here. From comparing Figs. 7.3 and 7.4 it is clear that the conductance pattern has completely changed. The horizontal lines around $V_{sd} = \pm 0.20\,\mathrm{mV}$ in Fig. 7.4 correspond to the superconducting gap of 2Δ, and mark the onset of direct quasi-particle tunneling between source and drain. These lines continue throughout the whole measured gate range, fluctuating slightly with varying V_g, and have been observed for all 14 samples studied. The appearance of a subgap structure at $V_{sd} \leq 2\Delta$ can be understood by invoking multiple Andreev reflection (MAR) at the boundaries of the superconducting leads and the quantum dot [12, 13]. Andreev reflection is a higher-order tunneling process in which an incident electron is converted into a Cooper pair, leaving a reflected hole in the normal region (see Fig. 7.4c). Andreev reflection has been studied extensively in mesoscopic devices such as thin wires or break junctions [14] in which electron-electron interaction and energy-level quantization can be

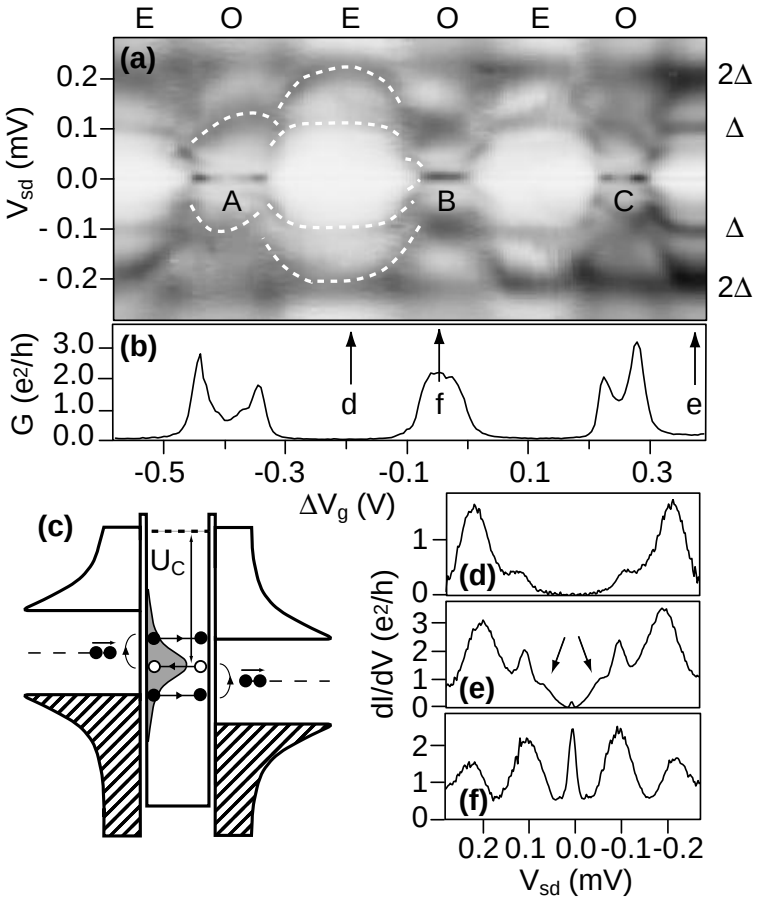

Figure 7.4: **(a)** Grey-scale representation of the differential conductance as function of V_{sd} and V_g at $T = 50\,\mathrm{mK}$ and $B = 0\,\mathrm{mT}$ for the same gate region as in Fig. 7.3. The dotted white lines indicate the shift of the Andreev peaks. **(b)** Linear-response conductance G as a function of V_g. **(c)** Schematics (simplified) of a quantum dot between superconductors showing two Andreev reflections. **(d-f)** dI/dV versus V_{sd} for the V_g positions indicted by the arrows in panel (b).

neglected.

In a quantum dot, however, Coulomb interaction cannot be neglected and is expected to suppress higher-order MAR [78, 71]. It is evident from Fig. 7.4 that the current through the dot also crucially depends on the level position of the electron states and on the number of electrons on the dot, having total spin $S = 0$ or $S = 1/2$. Note that both $U_C, \delta E > 2\Delta$ in the gate range of Fig. 7.4 and only a single level is expected to be present within a bias window 2Δ.

We will first discuss the conductance behavior in the even diamonds ($S = 0$). In the normal state the conductance has a relatively large value of $\sim 0.5\, e^2/h$ in the middle of the diamonds but becomes suppressed when the leads are superconducting, see Fig. 7.4d-e. Whereas in the normal state second-order elastic co-tunneling processes can contribute significantly to the conductance in our device, this is no longer allowed in the superconducting state due to the opening of an energy gap in the leads. Only higher-order MAR processes can give rise to a finite conductance at small bias. The dominant order n depends on V_{sd} as $2\Delta/en \leq V_{sd} \leq 2\Delta/e(n-1)$ and is therefore large when V_{sd} is small. This leads to a rapid decay of the linear-response conductance when a single-electron state is tuned away from the Fermi energy of the leads and G almost completely vanishes in the middle of the diamonds. When V_{sd} is increased, lower-order MAR processes become possible. Indeed at $V_{sd} \approx 0.10\,\mathrm{mV}$ (Δ/e) the current increases (see peaks in the dI/dV in Figs. 7.4d-f), corresponding to the opening of a channel with one Andreev reflection ($n = 2$). In Fig. 7.4e peaks in the dI/dV at even lower V_{sd} can be observed (arrows), probably involving a process with two Andreev reflections ($n = 3$), shown schematically in Fig. 7.4c.

It is interesting to note that, as indicated in Fig. 7.4a by the dotted white lines, the Andreev peaks appear to shift in energy as V_g is changed. This is unique for quantum dots and related to the shift of the level position of the single-electron states with V_g [79, 80]. A detailed comparison of the observed energy dependence of the MAR peaks with theory is discussed in section 7.3.

For the odd diamonds ($S = 1/2$) the situation is different. In the normal state the source and drain electrode are strongly coupled by virtue of the Kondo effect. The lowest-order process in the normal state, where one electron on the dot is replaced by another one with opposite spin, is no longer directly possible in the superconducting state since each such process must necessarily break a Cooper pair. One might therefore expect the Kondo effect to be suppressed when the leads become superconducting. Indeed, the conductance in the middle of two of the Kondo ridges (A and C) diminishes in the superconducting state. The conductance of Kondo ridge B, however, is actually *enhanced* and a narrow resonance remains around

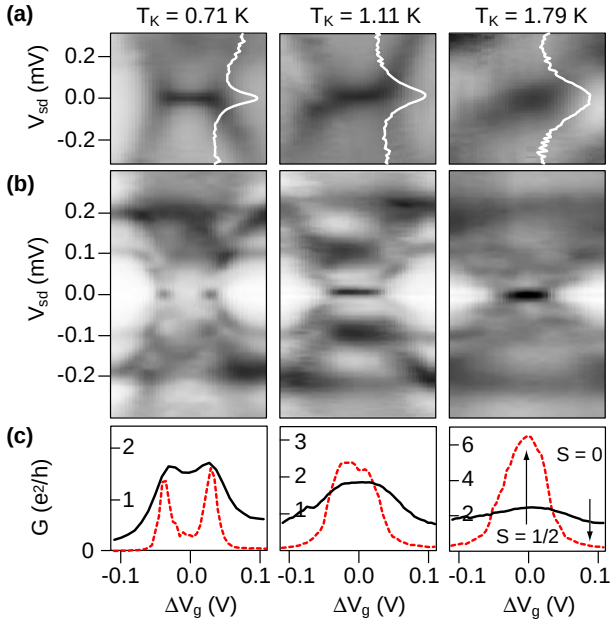

Figure 7.5: **(a)** dI/dV grey-scale plot for 3 different Kondo ridges at $T = 50\,\mathrm{mK}$ and $B = 26\,\mathrm{mT}$. The dI/dV_{sd} versus V_{sd} traces are measured in the middle of the ridges. **(b)** The same plot for the superconducting state. An intricate patterns develops showing multiple Andreev peaks, the position and magnitude of which depend on the level position. **(c)** Linear-response conductance in the normal (solid line) and superconducting (dashed line) state. The rightmost plot shows that even if the conductance modulation in the normal state is weak and $G \sim 2\,e^2/h$ both for $S = 0$ and $S = 1/2$, the difference can be dramatic when the leads are superconducting.

$V_{sd} = 0\,\mathrm{mV}$, see Fig. 7.4f. Note that ridge B has a higher T_K than those of A and C. These observations are in accordance with theoretical predictions which state that the Kondo resonance should *not* be destroyed by the superconductivity if T_K is sufficiently large [81, 82, 83]. More precisely, a cross-over is expected for $k_B T_K \sim \Delta$.

The Kondo temperature varies from level to level reflecting the fact that the wave functions of the particular quantum states can have different overlaps with the electrodes. Since we observe a multitude of Kondo resonances in our MWNT quantum dot, having a variety of T_K's we are able to test the theoretical predictions mentioned above. The width (FWHM) of the observed Kondo ridges, corresponding to $k_B T_K/e$, ranges between 0.045 and

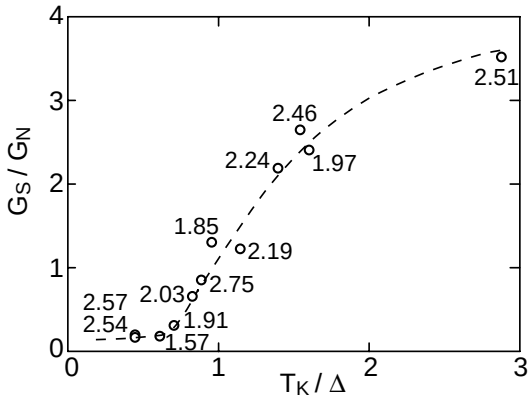

Figure 7.6: The data points give the ratio G_S/G_N of the conductances in the middle of 12 different Kondo ridges in the superconducting (G_S) and normal (G_N) state versus T_K/Δ measured at $T = 50\,\mathrm{mK}$. The gap energy Δ is 0.1 meV, corresponding to 1.16 K. The numbers indicate G_N in units of e^2/h for each data point. The fact that G_N can reach values as high as $2.7\,e^2/h$ implies that more than 1 level can contribute to the current. The dashed line is a guide to the eye.

0.29 mV. The superconducting gap is a constant ($\Delta/e \approx 0.10\,\mathrm{mV}$), which means that the ratio of both numbers can both be slightly larger or smaller than 1 depending on the particular level. In Fig. 7.5 we show 3 different Kondo ridges with increasing T_K from left to right. The conductance in the middle of the narrowest ridge is clearly suppressed when the leads become superconducting. At the other end of the spectrum, however, a pronounced increase can be observed. This can be understood qualitatively considering that in the latter case the energy necessary to break a Cooper pair, which is proportional to Δ, is more than compensated for by the formation of the Kondo singlet, having a binding energy of $\sim k_B T_K$. The Kondo state now provides a strong coupling between superconducting electrodes and the conductance can increase far beyond its normal-state value [84]. No supercurrent branch has been observed, which we attribute to quantum and thermal fluctuations in our device [85]. In Fig. 7.6 we show the ratio of the conductances in the superconducting and normal state, G_S/G_N, versus T_K/Δ for all measured Kondo resonances (see also App. C). The cross-over between increased and suppressed conductance indeed appears at $T_K/\Delta \sim 1$, consistent with the theoretical predictions.

The present study has shown detailed transport measurements of a carbon nanotube quantum dot coupled to superconducting leads. Exactly such systems are presently considered as excellent candidates for the creation of

nonlocal spin-entangled electron pairs [86, 87]. In these proposals the superconductor acts as a natural source of entangled electrons (the Cooper pairs) and the repulsive interaction in the nanotubes can be exploited to spatially separate the electrons of a pair. Future research will explore this important topic further.

7.3 Multiple Andreev reflections in a quantum dot

The electronic transport properties of quantum dots coupled to metallic leads have been the object of extensive theoretical and experimental study [10]. When weakly coupled to its leads, the low-temperature transport characteristics of a quantum dot are usually dominated by size and charge quantization effects, parameterized by the single-electron level spacing ΔE and the single-electron charging energy U_C. When the coupling of the quantum dot to the source and drain electrodes is increased, higher-order tunneling processes such as the Kondo effect become important [48]. New effects are expected when the leads coupled to the quantum dot are superconductors. In that case electron transport is mediated by multiple Andreev reflection (MAR) [12, 13]. Unlike conventional S-N-S devices, however, the MAR structure is now expected [79, 80] to strongly depend on the level positions of the single-electron states of the quantum dot which can be tuned with a gate electrode. The influence of Coulomb and Kondo correlations have been addressed theoretically in Refs. [83, 88].

Because MAR is suppressed rapidly for low-transparency junctions, its observation requires a relatively strong coupling between the leads and quantum dot. Even more so as on-site Coulomb repulsion, which is common to weakly coupled dots, is expected to reduce Andreev processes even further. A quantum dot very weakly coupled to superconducting leads has been studied experimentally by Ralph *et al.* [78]. In this case the transport characteristics were indeed dominated by charging effects and MAR was completely suppressed.

The coupling to the leads, expressed in the life-time broadening Γ of the quantum dot levels, should be compared to the superconducting gap energy Δ. Favourable for the observation of MAR in a quantum dot are coupling strengths of order $\Gamma \sim \Delta$ and a small charging energy $U_C < \Delta$. Together with the restriction that $\Gamma < \Delta E$ (for any quantum dot) this leads to the approximate condition $U_C \lesssim \Gamma \lesssim \Delta E$. For most quantum dots typically the opposite is true and $\Delta E \ll U_C$. It has recently been shown [89] however, that well-coupled multiwall carbon nanotube (MWNT) quantum dots can have favourable ratio's of $\Delta E/U_C \sim 2$ and U_C can be as small as 0.4 meV, comparable to the energy gap 2Δ of a conventional superconductor like Al.

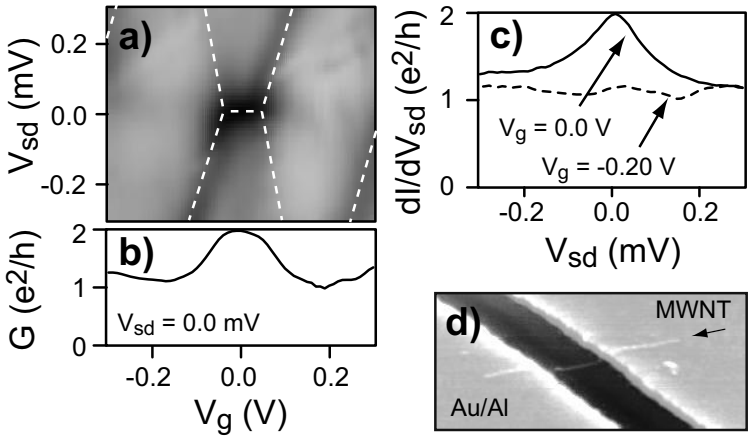

Figure 7.7: **(a)** Grey-scale representation of the differential conductance as a function of source-drain (V_{sd}) and gate voltage (V_g) at $T = 50\,\mathrm{mK}$ and $B = 26\,\mathrm{mT}$ for a MWNT quantum dot (darker = more conductive). **(b)** Linear-response conductance G as a function of V_g. The appearance of a single broad peak is due to the Kondo effect. **(c)** Differential conductance at two different values of V_g. **(d)** Typical device geometry. For the measurements presented here, the electrode spacing is 250 nm and the MWNT length 1.5 μm. The Si substrate is used as a gate electrode.

Here we report on the experimental study of resonant MAR in a MWNT quantum dot. The superconducting leads to the MWNT consist of an Au/Al bilayer (45/135 nm) deposited on top of the nanotube (see Fig. 7.7d). Before investigating the system in the superconducting state, the sample is first characterized in the normal state by applying a small magnetic field. From these measurements relevant parameters such as ΔE, U_C, and Γ are obtained. We then discuss a theoretical model that describes the differential conductance of an individual level in a quantum dot coupled to superconducting electrodes. In the final part of this section we compare the calculated differential conductance with the experimental data.

Figure 7.7 shows a grey-scale representation of the differential conductance dI/dV_{sd} versus source-drain (V_{sd}) and gate voltage (V_g) at $T = 50\,\mathrm{mK}$ when the contacts are driven normal by a small magnetic field. The dotted white lines outline the onset of first-order tunneling and appear when a discrete energy level of the quantum dot is at resonance with the electrochemical potential of one of the leads. From these and other electron states measured for this sample (about 20 in total), we obtain an average single-electron level spacing $\Delta E \sim 0.6\,\mathrm{meV}$ and a charging energy

$U_C \sim 0.4\,\mathrm{meV}$. Since $U_C = e^2/C_\Sigma$ this yields $C_\Sigma = 400\,\mathrm{aF}$ for the total capacitance which is the sum of the gate capacitance (C_g) and the contact capacitances C_s (source) and C_d (drain). From the data of Fig. 7.7a we obtain $C_g/C_\Sigma = 0.0036$, and $C_s/C_d = 0.45$. The lifetime broadening Γ is obtained from the width of the single-electron peaks at finite source-drain voltage (taking the background conductance into account) and is found to be $\Gamma \sim 0.35\,\mathrm{meV}$.

The high-conductance ridge around $V_{sd} = 0\,\mathrm{mV}$ in Fig. 7.7a is a manifestation of the spin-1/2 Kondo effect occurring when the number of electrons on the dot is odd. As a result, the Coulomb valley in the conductance has disappeared in this region of V_g and at 50 mK, which is the base temperature of our dilution refrigerator, only a single peak remains, see Fig. 7.7b. The appearance of the Kondo effect is an indication that the coupling to the leads is relatively strong. We will not discuss the Kondo effect here, and instead refer to section 7.2 or Ref. [90].

When the magnetic field is switched off, the leads become superconducting. To calculate the expected differential conductance in the superconducting state of the leads we have used the non-equilibrium Green-function technique [91]. We model the quantum dot as a series of spin-degenerate resonant levels coupled to superconducting electrodes, which are assumed to have a BCS spectral density. Note that neither electron-electron interaction (Coulomb blockade) nor exchange correlations (Kondo effect) are accounted for in the model, which may, therefore, not explain all details of the actual measurements. However, the interplay between MAR and resonant scattering already leads to strongly nonlinear IV-characteristics and reproduces some of the key features of the data. The main parameters entering the calculation are the two tunneling rates $\Gamma_{s(d)}$ and Δ. In the model we account for the gate voltage by a shift of the levels, which can be adjusted according to the experimentally observed Coulomb diamonds, see Fig. 7.7.

The discrete nature of the single-electron states is most pronounced when Γ is small. Therefore, before presenting the model calculation that directly compares to the experimental data, we first discuss the transport characteristics of a single spin-degenerate level with a relatively weak and symmetric coupling to the superconducting leads along the lines of Refs. [79, 80]. The total tunneling rate $\Gamma \equiv \Gamma_s + \Gamma_d$ is set to Δ. Figure 7.8 shows the corresponding grey-scale representation of the calculated differential conductance dI/dV_{sd} versus $\varphi_g := eV_gC_g/C_\Sigma$ and eV_{sd}. The peak structure in dI/dV_{sd} at $V_{sd} < 2\Delta/e$ is the result of MAR. In general, Andreev channels become available for transport at voltages $V_{sd} = 2\Delta/ne$, where n is an integer number. These positions are indicated by the horizontal dashed black lines in Fig. 7.8a. The appearance and magnitude of the MAR peaks, however, is strongly dependent on the position of the resonant level in the quantum dot

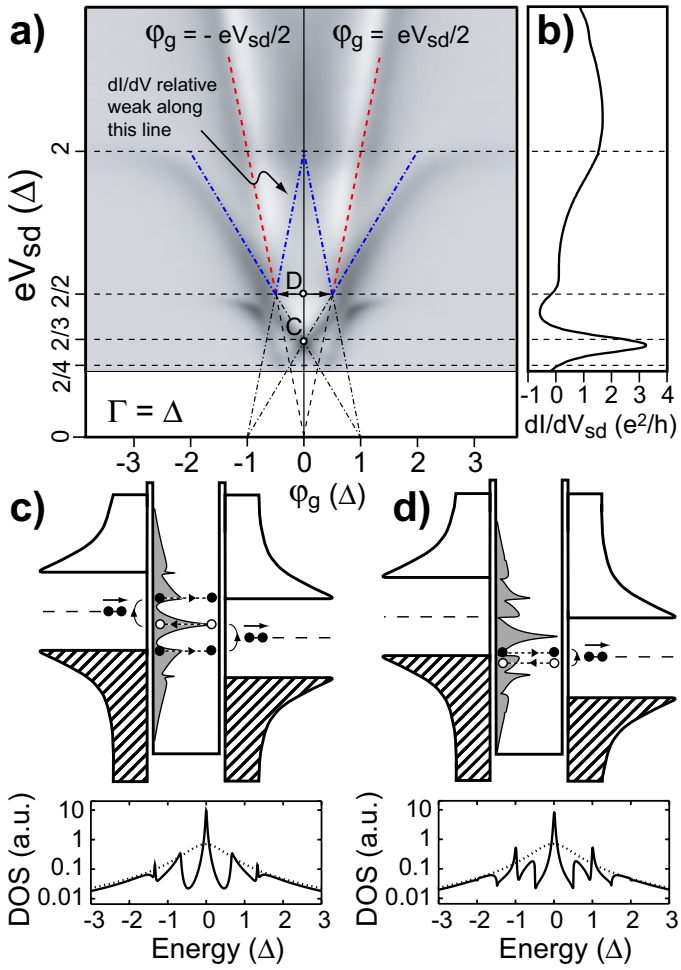

Figure 7.8: **(a)** Grey-scale representation of the calculated differential conductance as a function of V_{sd} and level position ($\varphi_g \propto V_g$) for a single-electron level coupled symmetrically to superconducting electrodes. For clarity, the low-energy part $eV_{sd} \lesssim 2\Delta/4$ has been omitted. The dashed lines indicate resonance positions, as explained in the text. **(b)** Differential conductance at $\varphi_g = 0$. Note that MAR peaks at $2\Delta/n$ are suppressed for even values of n. **(c)** Schematics of a single electron state between superconducting source and drain electrodes. The situation corresponds to point C in panel (a). The spectral density is shown at the bottom. The Lorentzian level in the normal state (dotted line) is replaced by a narrow central resonance accompanied by a series of satellite peaks.**(d)** Same as (c) for point D in panel (a).

with respect to the Fermi energy of the leads. Only those MAR trajectories that connect the resonant level to the leads' BCS spectral densities give a significant contribution to the current. Consider, for example, the position marked by C in Fig. 7.8a, which corresponds to the schematics of Fig. 7.8c and indicates the position $(\varphi_g, eV_{sd}) = (0, 2\Delta/3)$. The corresponding Andreev trajectory connects the gap edges of the source and drain electrodes and includes the resonant level which is situated exactly in between the respective Fermi energies. This results in the large peak in dI/dV_{sd} seen in Fig. 7.8b.

A similar peak is absent at $(\varphi_g, eV_{sd}) = (0, \Delta)$, corresponding to point D in Fig. 7.8a. Now, the corresponding trajectories (see Fig. 7.8d) do not directly connect the resonant level to the leads' spectral densities, and therefore do not significantly contribute to the current. Only when the gate voltage is adjusted to align the level with the Fermi energy of one of the leads (indicated by the arrows in Fig. 7.8a) a peak in dI/dV_{sd} is observed. It can be shown (for symmetric junctions) that the subharmonic gap structure at $V_g = 0$ is suppressed for all voltages $V_{sd} = 2\Delta/ne$ with $n =$ even [79, 80]. When V_{sd} is increased beyond Δ/e, peaks are observed either when the level stays aligned with the electrochemical potential of the leads (red dashed lines: $\varphi_g = \pm eV_{sd}/2$) or when the level follows the gap edges as an initial or final state of an Andreev process (blue dash-dotted lines: $\varphi_g = \pm(\Delta - eV_{sd}/2)$ or $\varphi_g = \pm(\Delta - 3eV_{sd}/2)$).

We now turn to the actual measurements of the differential conductance when the leads are in the superconducting state. Figure 7.9 shows a grey-scale representation of the measured dI/dV_{sd} versus V_{sd} and V_g at $B = 0\,\mathrm{mT}$ for the same single-electron state of Fig. 7.7. A number of differences between the normal state (Fig. 7.7) and superconducting state (Fig. 7.9) can be observed. The horizontal high-conductance lines at voltages $V_{sd} = \pm 0.2\,\mathrm{mV}$ in Fig. 7.9, for example, are attributed to the onset of quasi-particle tunneling when the voltage difference between the source and drain electrode equals $2\Delta/e$. The subgap structure at $V_{sd} < 2\Delta/e$ is attributed to MAR. As anticipated, the magnitude and the position (dashed white lines) of MAR peaks depend on V_g. To allow for comparison with theory, the adjustable parameters of the model are set to the values obtained from the measurement of Fig. 7.7. The most important parameter is the coupling between the electrodes and the dot which turns out to be $\Gamma \sim 3.5\ \Delta$. The voltage division between the two tunnel barriers separating the quantum dot from the leads is $C_s/C_d = 0.45$. The individual tunneling rates of the source and drain electrodes to the dot are not exactly known but are not expected to show a strong asymmetry since the Kondo resonance of Fig. 7.7 saturates at a value close to $2\,e^2/h$. The neighboring single-electron states, separated by $\Delta E \sim 6.5\Delta$, are included in the calculation. The finite temperature of

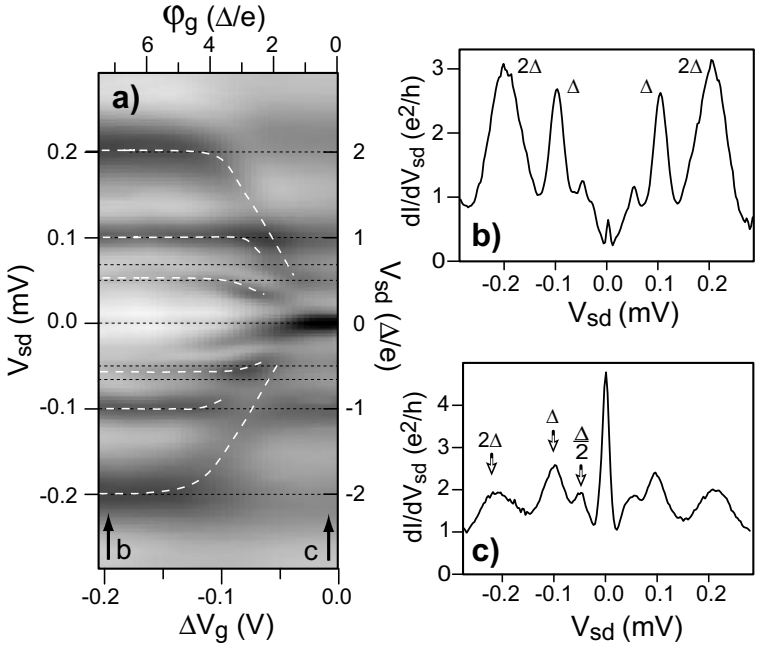

Figure 7.9: **(a)** Grey-scale representation of the measured differential conductance as a function of V_{sd} and V_g at $T = 50\,\mathrm{mK}$ with the leads in the superconducting state. The gate voltage range corresponds to the left part of Fig. 7.7a. The dashed white lines emphasize the position of the MAR peaks. **(b-c)** Differential conductance at the positions given in panel (a).

the experiment is taken into account and set to $T = 0.1\,\Delta$.

The resulting calculated grey-scale representation of the differential conductance is shown in Fig. 7.10. The overall appearance clearly resembles the measured data of Fig. 7.9. For example, both the model and the measured data show a large peak in dI/dV_{sd} around $V_{sd} = 0\,\mathrm{mV}$ when the electron state is at resonance with the electrochemical potential of the leads (i.e. at $V_g = 0$). When the level is moved away from this position, the linear-response conductance rapidly decays to values below its normal-state value. In contrast, the differential conductance peak at $V_{sd} = 2\Delta/e$ shows the opposite behavior (both in the model as in the experiment). At $V_g = 0$, this peak is much less pronounced than at lower values of V_g. These observations are similar to conventional S-N-S structures, such as atomic-sized break junctions [14]: For large transparencies of the junction a peak is observed at $V_{sd} = 0$ but no structure at 2Δ while for small transparencies a

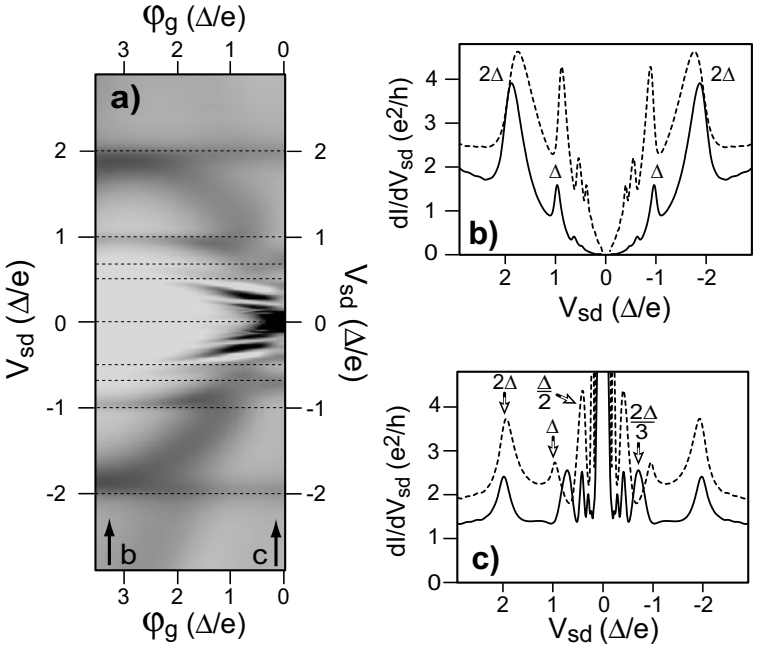

Figure 7.10: **(a)** Grey-scale representation of the calculated differential conductance as a function of V_{sd} and level position (φ_g). The different adjustable parameters represent the experimental situation, see text. **(b-c)** Differential conductance at the positions given in panel (a). For the two dashed curves, Γ has been chosen approximately twice as large as the experimental value.

gap is observed around $V_{sd} = 0$ and a large peak at 2Δ marks the onset of quasi-particle tunneling. In contrast to breakjunctions, for which the transparency depends on the atomic arrangement of the junction, the effective transparency can be tuned in a quantum dot by moving the level position through the gate electrode. The effective transparency is large if the level is aligned with the Fermi levels of the leads (on resonance) and it is small otherwise (off resonance).

The subharmonic gap structure is clearly visible in the measured data of Fig. 7.9 and has a similar gate-voltage dependence as in the model calculation of Fig. 7.10. However, there are several differences. The most dramatic one is the pronounced peak at $(V_g, V_{sd}) = (0, \Delta/e)$ in the measurement (Fig. 7.9c). Because this position corresponds to an even MAR cycle it should be absent based on our previous consideration (see Fig. 7.8d).

Let us compare theory and experiment by focussing on the dI/dV_{sd} lines

traces shown in Figs. 7.9b-c and Figs. 7.10b-c (solid curves). In panels (b) the dot level is off resonance, while it is on resonance in panels (c). For the former case, experiment and theory agree fairly well. The differences in MAR structure between model and experiment are much more pronounced at the resonance position. Whereas the experiment (Fig. 7.9c) reveals pronounced peaks at $\Delta/2$, Δ and 2Δ, the calculated dI/dV_{sd} (Fig. 7.10c, solid) reveals fine structure for small V_{sd} and pronounced peaks at $2\Delta/3$ and 2Δ. According to our previous discussion dI/dV_{sd} should indeed show a pronounced peak at $V_{sd} = 2\Delta/3e$, if the dot level is centered in the middle, i.e. for $\varphi_g = 0$ at point C in Fig. 7.8a and Fig. 7.8c. It rather appears in the experiment that, contrary to expectations, the subgap feature at $2\Delta/3$ is missing, while the 'forbidden' at Δ is present. Such behavior would be expected only for very asymmetric junctions having $C_s/C_d \ll 1$ [92], which is not the case in the present work.

There are different imaginable scenarios that may account for the observed Δ peak and the lack of fine structure around $V_{sd} = 0\,\mathrm{mV}$ in the data of Fig. 7.9c. Inelastic scattering processes inside the dot, for example, would broaden and obscure higher-order MAR features. Other possible reasons may be found in a broadened BCS spectral density (the superconductor consists of a bilayer of Au/Al [70]) or a suppression of higher-order MAR due to the on-site Coulomb repulsion.

In a phenomenological approach, we may try to account for the additional broadening by manually introducing larger bare couplings $\Gamma_{s,d}$. Many curves with varying parameters were calculated of which a representative set is displayed in Fig. 7.10b-c (dashed curves) corresponding to relatively large dot-electrode couplings of $\Gamma_s = 2.5\,\Delta$ and $\Gamma_d = 3.5\,\Delta$. For the off-resonance position (Fig. 7.10b) the main effect of the larger Γ is the increased magnitude of dI/dV_{sd}. In contrast, the MAR structures significantly changes for the resonance position (Fig. 7.10c). Remarkably, at large coupling Γ, peaks now appear at 2Δ, Δ and $\Delta/2$. These peaks do not originate from the resonant level, but from the two neighboring ones which are off resonance (the dot levels are spaced by $\Delta E \approx 6.5\,\Delta$). Though the agreement is now reasonable, there is one remaining problem. We were unable to reproduce the relative peak height between the 2Δ and Δ peaks. Using any reasonable set of parameters, the 2Δ peak is always larger than the Δ peak in the model, while it is the opposite in the experiment. We emphasize that the model does not take into account interaction and correlations. Since a Kondo resonance is observed in the normal state, which need not be suppressed in the superconducting state [90], this may be the origin of the discrepancy. The Kondo resonance changes the spectral density in the leads by adding spectral weight to the center of the gap and removing spectral weight from the gap edges. The former tends to enhance the Δ peak, while the latter

tends to suppress the 2Δ one. This explanation is attractive, but more work both in theory and experiment is needed to substantiate it.

In conclusion, we have investigated the non-linear conductance characteristics of a quantum dot coupled to superconducting electrodes. We find a strong dependence of the MAR structure on the level position of the single-electron states. The experimental data is compared with a theoretical model, assuming a BCS density-of-states in the electrodes and an interaction-free dot. Reasonable agreement is possible, if the tunneling coupling to the leads is enhanced by a factor ~ 2 in the model as compared to the experimental value. There are additional subtle differences which point to the importance of interaction and exchange correlations.

Appendix A

Measurement cryostats

The low-temperature measurements have been performed in two different cryostats. Except for the measurements described in chapter 7 all experiments were done in a ^{3}He cryostat from Cryogenics with a base temperature of 280 mK. The second cryostat is an Oxford TLM 400 dilution refrigerator with an electron base temperature of about 50 mK.

^{3}He Cryostat

Figure A.1 shows (parts of) the ^{3}He cryostat used in our experiments. The ^{3}He is contained in a closed space and can be condensed at the '1 Kelvin pot' when cooled below about 2 K. In turn, the samples can be cooled to a base temperature of 280 mK by pumping away the ^{3}He vapour of the ^{3}He condensate using an charcoal adsorption pump which adsorbs ^{3}He molecules when cooled below 20 K. The samples can be kept cold at the base temperature for about 20 hours after which the ^{3}He has to be recondensed. The system is equipped with a π-filter stage at room temperature and thermocoax filters at low temperature.

Dilution refrigerator

The dilution refrigerator is based on the fact that below a critical temperature (860 mK) a mixture of ^{3}He and ^{4}He spontaneously separates into two phases, one rich in ^{3}He and one rich in ^{4}He. Cooling is obtained by 'evaporating' the ^{3}He from the rich phase into the dilute phase, similar to an ordinary vapour/liquid system. To obtain a continuous operation the ^{3}He atoms that pass through the phase boundary are pumped away and led back into the mixture through a condensor stage. The dilution refrigerator used in our experiments is an Oxford TLM 400 with a top loading

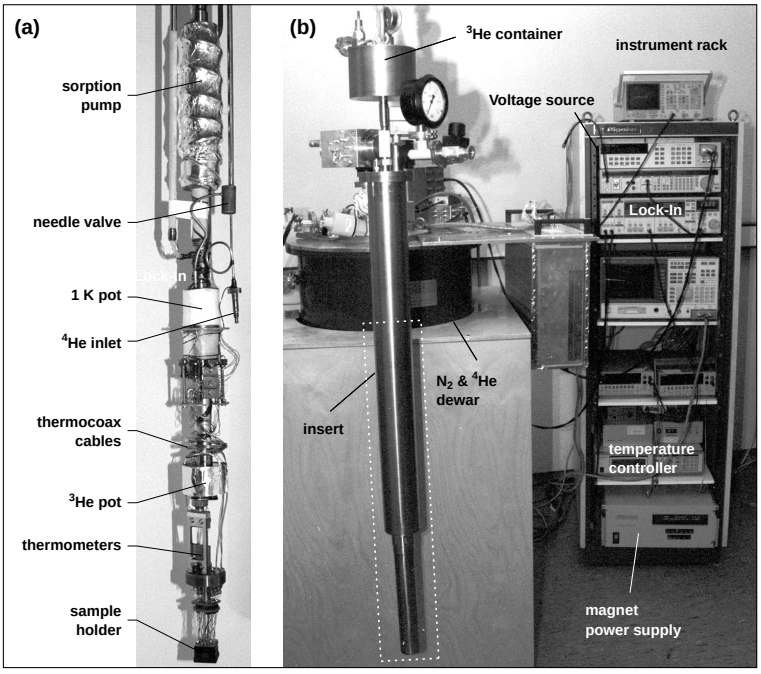

Figure A.1: **(a)** Low-temperature part of the ^{3}He insert with the tube for the isolation vacuum removed. **(b)** ^{3}He cryostat with instrument rack.

sample probe. The turn-around-time is approximately 10 hours. The mixing chamber base temperature is 28 mK. The electron base temperature has been determined from the shape of Coulomb blockade peaks (see below) and yielded $\sim$ 50 mK. To achieve the low electron temperature the wiring had to be filtered carefully. At room temperature the system has been equipped with two π-filter stages. At low temperatures all wires (8 sample and 4 thermometer wires) include about 100 cm of 'lossy' coaxial cable, see Fig. A.2. The sample is mounted in a RF tight brass box. In addition, the sample holder has been modified such that commercially available chip carriers can be inserted. As the top loading probe has a diameter of only 12 mm, the mounting of a new shielded sample holder, a calibrated thermometer and 12 separate lines of coaxial cable (requiring cadmium solder) has by no means been a straightforward task.

As mentioned above, the attenuation properties of a thin coaxial cable have been exploited as a low-temperature microwave filter. If the inner conductor and jacket are resistive enough, the losses in a coaxial cable increase as the square root of frequency due to the skin effect. In our system,

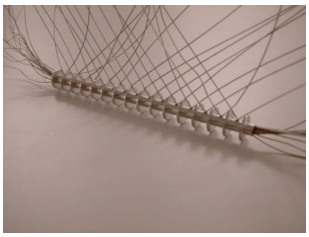

Figure A.2: The coaxial cables used as a low-temperature filter before the final assembly.

the central wire of the coaxial cable consisted of an IsaOhm resistive wire (NiCr20AlSi) of 0.23 mm diameter coated with 0.06 mm of insulating varnish (dielectric constant $\epsilon = 3.3$). The wire has an almost temperature independent resistivity of $1.32\,\mu\Omega$m. The jacket had been made of stainless steel (Goodfellow, resistivity of $0.71\,\mu\Omega$ m) with an inner diameter of 0.38 mm and an outer diameter of 0.5 mm. The space in between the central wire and jacket has been filled with paraffin. An estimate of the attenuation at 20 Ghz for this geometry is at least ~ 150 dB [93].

Figure A.3 shows the width (FWHM) of a Coulomb peak of a very weakly coupled MWNT having $G \ll e^2/h$. The peaks of this device were well separated at the temperature range of the dilution fridge (see inset). A linear decrease of the peak widths is observed down to $T \sim 50\,\mathrm{mK}$. The slope of this curve should follow the relation $\Delta V_g = 3.5 k_B T/\alpha e$, where α is the gate voltage-to-energy conversion factor given by the ratio of the gate and total capacitance C_g/C_Σ. The slope indicates an α of 1/150 in reasonable agreement with estimates of α from the Coulomb diamond patterns in the differential conductance measurements.

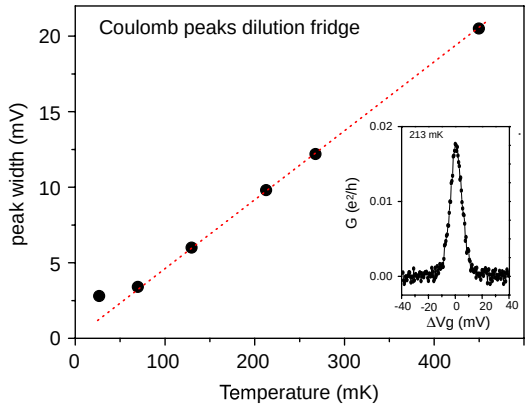

Figure A.3: Width of Coulomb peaks (FWHM) of a very weakly coupled MWNT quantum dot versus temperature. A linear decrease of the peak widths is observed down to $T \sim 50\,\mathrm{mK}$. The inset shows a Coulomb peak at 213 mK.

Appendix B

Freestanding MWNTs and shell burning

Preliminary tests have been performed to fabricate freestanding MWNT devices and to remove individual shells of the MWNTs. To this effect, a wet etch has been used to remove 200 nm of the SiO_2 substrate of the nanotube devices following the simple procedure of Ref. [94]. A buffered HF etch (10 % HF, etch rate 200 nm/3 min.) was used to suspend the nanotubes. After the HF etch the devices are transferred to de-ionized water followed by isopropanol.

Due to the high rigidity of MWNTs (as compared to e.g. SWNTs) the rate of successful suspension of the MWNTs with a 400 nm gap between electrodes is nearly 100 %. Room temperature measurements indicate that the HF etch leaves the MWNTs and Ti/Au electrodes unaffected as the 2-terminal resistance values of etched devices show no apparent difference compared to regular devices. Scanning electron microscope images of an etched MWNT device are shown in Fig. B.1. Freestanding carbon nano-

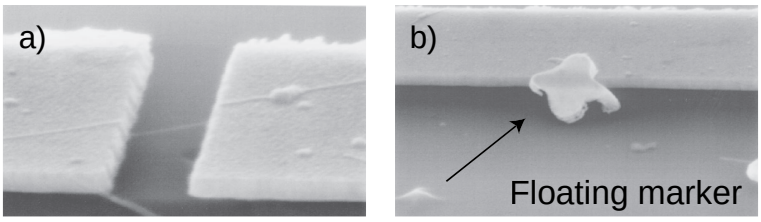

Figure B.1: **(a)** SEM image of a freestanding MWNT. Approximately 200 nm of the SiO2 substrate has been removed using a buffered HF etch. **(b)** This floating alignment marker clearly illustrates the achieved SiO_2 etch.

tubes of different lengths and diameter can be useful e.g. as templates for evaporating metallic nanowires [95] or as high frequency nanometer scale mechanical resonators [96].

The MWNTs can support a remarkable large current before electrical breakdown occurs. When the contact resistance is sufficiently low (of order 1 kΩ) the MWNTs fail via a series of equally sized current steps, as first observed in Ref. [97]. An example of the electrical breakdown of a free-standing MWNT in air is shown in Fig. B.2. Here the applied voltage over the MWNT could be raised to ~ 2.3 V at which the current saturated at a value of 140 μA (not shown). When the voltage is increased above the threshold voltage of 2.3 V the individual shells fail and the current decreases in steps of about 15 μA. Current saturation around a value of $15 - 25\,\mu$A has been observed first for SWNTs and attributed to electron-phonon scattering processes [98]. In the example of Fig. B.2 each individual shell of the MWNT indeed contributes to the saturation current with $\sim 15\,\mu$A. This would correspond to 8 to 10 current carrying MWNT shells.

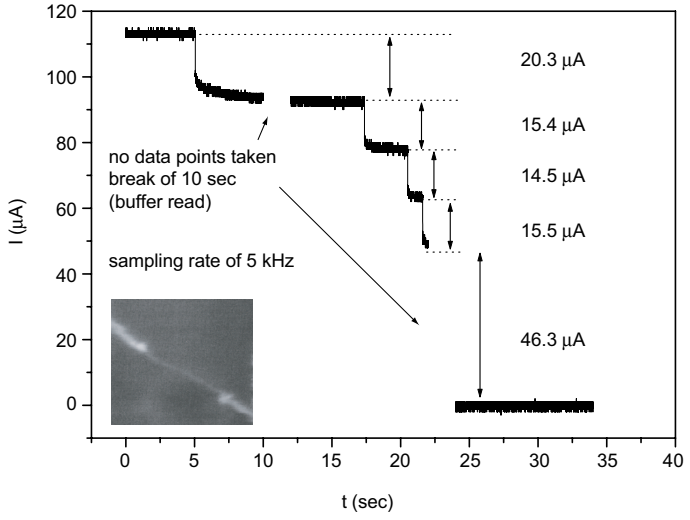

Figure B.2: Time trace of the measured current during a MWNT breakdown in air. The MWNT fails in steps of approximately 15 μA. No data points were taken at the positions indicated by the arrows which lasted about 10 seconds. The sampling rate of 5 kHz has been sufficient to resolve the steps. The insets shows a significant thinning in the middle of the MWNT after the experiment.

Appendix C

Additional Kondo data

Normal state

The Kondo resonances observed in chapters 5 and 7 are expected to show a linear splitting into components at $V_{sd} = \pm g\mu_B B/e$ when a magnetic field is applied, i.e. the total separation of the components is twice the Zeeman energy. Although the Kondo resonance described in chapter 5 indeed broadens and disappears when a magnetic field is applied, a clear splitting could not be resolved. This is different for the measurements presented in chapter 7 obtained at a lower base temperature of $T = 50\,\mathrm{mK}$. Here the splitting into two components is clearly visible as illustrated in Fig. C.1.

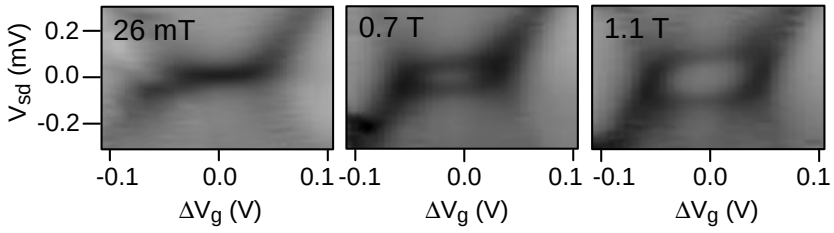

Figure C.1: Shown in a grey-scale representation of the differential conductance versus gate (ΔV_g) and source-drain voltage (V_{sd}) is the splitting of a Kondo resonance in a magnetic field at $T = 50\,\mathrm{mK}$ (darker = more conductive). This Kondo resonance is part of the measurement series on the MWNT device presented in chapter 7, see e.g. Fig 7.3.

Superconducting state

As discussed in section 7.2, the ratio G_S/G_N of the conductances in the middle of a Kondo ridge in the superconducting (G_S) and normal state (G_N) of the leads crosses unity when $k_B T_K \sim \Delta$. The gradual cross-over between the regimes of increased and suppressed conductance has been shown in Fig. 7.6 which plotted points of G_S/G_N versus T_K/Δ for different Kondo ridges. The value of G_S of each of these points has been obtained using graphs like Fig. C.2 which shows a grey-scale representation of the differential conductance with the leads in the superconducting state for a Kondo ridge having $T_K = 0.96\,\mathrm{K}$. The Kondo temperature of 0.96 K is slightly smaller than the superconducting gap energy $\Delta \approx 0.1$ meV which corresponds to 1.16 K. Indeed, the conductance is found to be suppressed in the middle of the Kondo ridge when the leads are superconducting as compared to the normal state (here $G_S/G_N \sim 0.65$). Even so, a small resonance is still visible. In fact, the resonance around $V_{sd} = 0\,\mathrm{mV}$ in the superconducting state of the leads gradually develops when the Kondo temperature increases. This is most clearly illustrated in Fig. C.3 which shows an emerging Kondo resonance with increasing T_K for 10 different ridges.

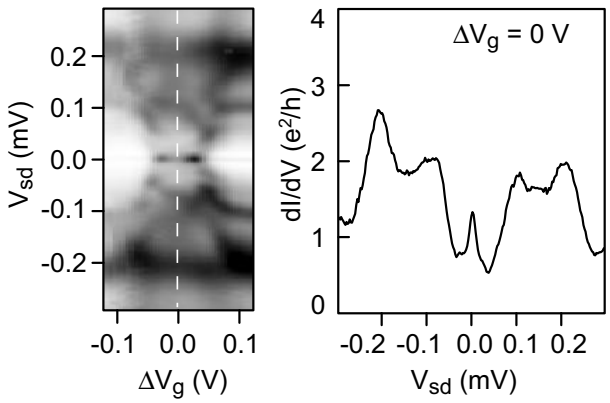

Figure C.2: Grey-scale representation of the differential conductance in the superconducting state of the leads for a Kondo resonance having $T_K = 0.96\,\mathrm{K}$. The line trace shows the differential conductance evaluated along the dashed line at $\Delta V_g = 0\,\mathrm{V}$.

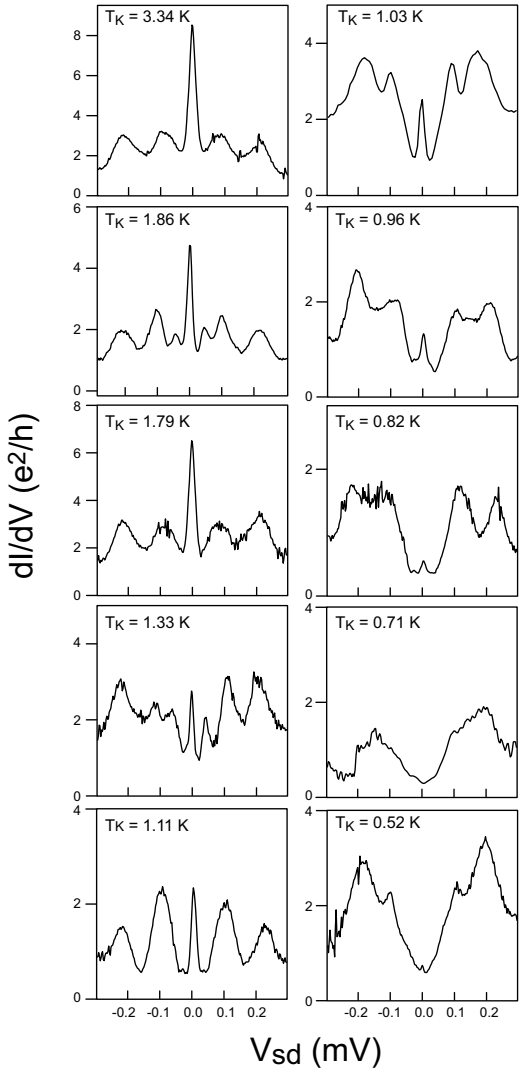

Figure C.3: Differential conductance in the middle of 10 different Kondo ridges when the leads are in the superconducting state. The measurements are obtained at a temperature of $T = 50\,\mathrm{mK}$.

Magnetic field dependence

The magnetic field dependence at small fields is shown in Fig. C.4. The top and bottom plots are obtained at two different positions of the gate voltage for the MWNT device described in sections 7.2 and 7.3. The top plot shows a position in the middle of a Coulomb diamond having total spin S=0. The critical field appears to be $\sim$ 12 mT. Above this field the differential conductance is featureless and has a relatively low value of $0.5\,e^2/h$. When the field is decreased a gap opens, the linear-response conductance vanishes and Andreev structure appears. The slight shift of the center to 3 mT is probably due to a small remanent field. When in chapter 7 the devices are said to be studied in the superconducting state at $B = 0$ T, the magnetic field is actually carefully tuned to be at the position where the superconducting gap is maximum (here at around 3 mT). The bottom plot of Fig. C.4 is near (but not exactly at) the center of a Kondo resonance. As before, the normal state properties are retained above $\sim$ 12 mT. When the field is decreased the Kondo resonance is transformed into a narrow resonance accompanied by Andreev peaks at higher V_{sd}.

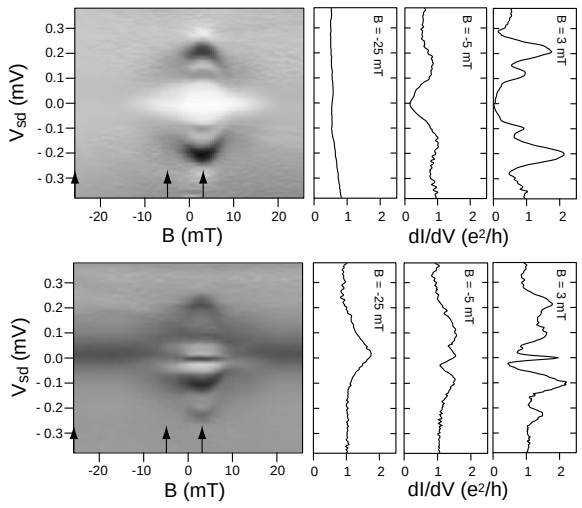

Figure C.4: Grey-scale representations of the differential conductance versus field and source-drain voltage for $T = 50\,\mathrm{mK}$ (darker = more conductive). The top and bottom plots are for 2 different gate position. The top plot is in the middle of an $S = 0$ Coulomb diamond, whereas the bottom plot is near, but not exactly at, a Kondo resonance ($T_K = 1.11\,\mathrm{K}$, see e.g Fig. C.3). The line traces show dI/dV at the positions of the arrows.

Bibliography

[1] S. Iijima, Nature **354**, 56 (1991).

[2] S. Iijima and T. Ichihashi, Nature **361**, 603 (1993).

[3] M. S. Dresselhaus, G. Dresselhaus, and P. C. Eklund: *Science of Fullerenes and Carbon Nanotubes* (Academic Press, New York 1996).

[4] R. Landauer, IBM J. Res. Dev. **1**, 223 (1957).

[5] M. Büttiker, Phys. Rev. Lett. **57**, 1761 (1986).

[6] C.W.J. Beenakker and H. van Houten, *Quantum Transport in Semiconductor Nanostructures*, edited by H. Ehrenreich and D. Durnbull (Academic Press, New York, 1991).

[7] G. Bergmann, Phys. Rep. **107**, 1 (1984).

[8] S. Datta, *Electronic Transport in Mesoscopic Systems* (Cambridge University Press, Cambridge 1995).

[9] H. Grabert and M.H. Devoret (eds.), *Single Charge Tunneling* (Plenum, New York, 1992).

[10] L.P. Kouwenhoven *et al.*, in *Mesoscopic Electron Transport,* edited by L.L. Sohn *et al.* (Kluwer, Dordrecht, The Netherlands, 1997).

[11] M. Tinkham, *Introduction to Superconductivity* (McGraw-Hill, New York, 1996), 2nd ed.

[12] A.F. Andreev, Sov. Phys. JETP **19**, 1228 (1964).

[13] M. Octavio, M. Tinkham, G.E. Blonder, and T.M. Klapwijk, Phys. Rev. B. **27**, 6739 (1983).

[14] E. Scheer, P. Joyez, D. Esteve, C. Urbina, and M.H. Devoret, Phys. Rev. Lett. **78**, 3535 (1997).

[15] E. Scheer, N. Agraït, J.C. Cuevas, A. Levy Yeyati, B. Ludolph, A. Martín-Rodero, G.R. Bollinger, J.M. van Ruitenbeek, and C. Urbina, Nature **394**, 154 (1998).

[16] T.W. Ebbesen and P.M. Ajayan, Nature **358**, 220 (1992).

[17] J.M. Bonard, T. Stora, J-P. Salvetat, F. Maier, T. Stöckli, C. Duschl, L. Forró, W.A. de Heer, and A. Châtelin, Advanced Materials **9**, 827 (1997).

[18] J.W.G. Wildöer, L.C. Venema, A.G. Rinzler, R.E. Smalley, and C. Dekker, Nature **391**, 59 (1998)

[19] J.W. Mintmire, B.I. Dunlap, and C.T. White, Phys. Rev. Lett. **68**, 631 (1992).

[20] N. Hamada, S. Sawada, and A. Oshiyama, Phys. Rev. Lett. **68**, 1579 (1992).

[21] R. Saito, M. Fujita, G. Dresselhaus, and M.S. Dresselhaus. Appl. Phys. Lett. **60**, 2204 (1992).

[22] P.R. Wallace, Phys. Rev. **71**, 622 (1947).

[23] C.T. White and J.W. Mintmire, Nature **391**, 19 (1998).

[24] T. Ando, T. Nakanishi, and R. Saito, J. Phys. Soc. Jpn. **67**, 2857 (1998);

[25] T. Ando and T. Nakanishi, J. Phys. Soc. Jpn. **67**, 1704 (1998).

[26] P.L. McEuen, M. Bockrath, D.H. Cobden, Y. Yoon, and S.G. Louie, Phys. Rev. Lett. **83**, 5098 (1999).

[27] T.W. Odom, J.-L. Huang, P. Kin, and C. Lieber, Nature **391**, 62 (1998).

[28] L.C. Venema, J.W. Janssen, M.R. Buitelaar, J.W.G. Wildöer, S.G. Lemay, L.P. Kouwenhoven, and C. Dekker, Phys. Rev. B **62**, 5238 (2000).

[29] S.J. Tans, A.R.M. Verschueren, and C. Dekker, Nature **393**, 49 (1998).

[30] R. Martel, T. Schmidt, H.R. Shea, T. Hertel, and Ph. Avouris, Appl. Phys. Lett. **73**, 2447 (1998).

[31] C. Schönenberger, A. Bachtold, C. Strunk, J.-P. Salvetat, and L. Forró, Appl. Phys. A **69**, 283 (1999).

[32] A. Bachtold, C. Strunk, J.-P. Salvetat, J.-M. Bonard, L. Forró, T. Nussbaumer, and C. Schnenberger, Nature **397**, 673 (1999).

[33] J. Kong, N.R. Franklin, C. Zhou, M.G. Chapline, S. Peng, K. Cho, and H. Dai, Science **287**, 622 (2000).

[34] P.G. Collins, K. Bradley, M. Ishigami, and A. Zettl, Science **287**, 1801 (2000).

[35] S.-H. Jhi, S.G. Louie, and M. Cohen, Phys. Rev. Lett. **85**, 1710 (2000).

[36] A. Bachtold, P. Hadley, T. Nakanishi, and C. Dekker, Science **294**, 1317 (2001).

[37] P.G. Collins, M.S. Arnold, and P. Avouris, Science **292**, 706 (2001).

[38] B. L. Altshuler, Pis'ma Zh. Eksp. Teor. Fiz. **41**, 530 (1985) [JETP Lett. **41**, 648 (1985)]; P.A. Lee and A.D. Stone, Phys. Rev. Lett. **55**, 1622 (1985); P.A. Lee, A.D. Stone, and H. Fukuyama, Phys. Rev. B **35**, 1039 (1987).

[39] B.L. Altshuler, A.G. Aronov, D.E. Khmelnitsky, J. Phys. C **15**, 7367 (1982).

[40] P.M. Echternach, M.E. Gershenson, H.M. Bozler, A.L. Bogdanov, B. Nilsson, Phys. Rev. B **48**, R11516 (1993); Y.B. Khavin, M.E. Gershenson, A.L. Bogdanov, Phys. Rev. Lett. **81**, 1066 (1998).

[41] W. Liang, M. Bockrath, D. Bozovic, J.H. Hafner, M. Tinkham, and H. Park, Nature **411**, 665 (2002).

[42] M. Krüger, M.R. Buitelaar, T. Nussbaumer, and C. Schönenberger, Appl. Phys. Lett. **78**,1291 (2001).

[43] S. J Tans, M. H. Devoret, H. Dai, A. Thess, R. E. Smalley, L. J. Geerligs, and C. Dekker, Nature **386**, 474 (1997).

[44] M. Bockrath, D. H. Cobden, P. L. McEuen, N. G. Chopra, A. Zettl, A. Thess, and R. E. Smalley, Science **275**, 1922, (1997).

[45] J. Nygård, Ph.D. thesis, University of Copenhagen, (2000).

[46] S. Tarucha, D.G. Austing, Y. Tokura, W.G. van der Wiel, and L.P. Kouwenhoven, Phys. Rev. Lett. **84**, 2485 (2000).

[47] D. H. Cobden, M. Bockrath, P.L. McEuen, A.G. Rinzler, and R.E. Smalley, Phys. Rev. Lett. **81**, 681 (1998).

[48] L. Kouwenhoven and L. Glazman, Phys. World, **14**, No. 1, 33-38 (2001).

[49] J. Nygård, D.H. Cobden, and P. E. Lindelof, Nature **408**, 342 (2000).

[50] S. De Franceschi, S. Sasaki, J.M. Elzerman, W.G. van der Wiel, S. Tarucha, and L.P. Kouwenhoven, Phys. Rev. Lett. **86**, 878 (2001).

[51] C. T. White and T. N. Todorov, Nature **393**, 240 (1998).

[52] A. Bachtold, M. S. Fuher, S. Plyasunov, M. Fuhrer, E. H. Anderson, A. Zettl, and P. L. McEuen, Phys. Rev. Lett. **84**, 6082 (2000).

[53] M. P. A. Fisher, L. I. Glazman in *Mesoscopic Electron Transport,* edited by L.L. Sohn *et al.* (Kluwer, Dordrecht, The Netherlands, 1997); J. Voit, Rep. Prog. Phys. **57**, 977 (1995).

[54] R. Egger and A. O. Gogolin, Phys. Rev. Lett. **79**, 5082 (1997); C. Kane, L. Balents, and M. P. A. Fisher, Phys. Rev. Lett. **79**, 5086 (1997).

[55] M. Bockrath, D. H. Cobden, Lu Jia, A. G. Rinzler, R. E. Smalley, L. Balents, and P. L. McEuen, Nature **397**, 598 (1999).

[56] Z. Yao, H. W. C. Postma, L. Balents, and C. Dekker, Nature **402**, 273 (1999).

[57] H. W. C. Postma, M. de-Jonge, and C. Dekker, Phys. Rev. B **62**, R10653 (2000).

[58] L. Langer, V. Bayot, E. Grivei, J.-P. Issi, J. P. Heremans, C. H. Olk, L. Stockman, C. Van-Haesendonck, and Y. Bruynseraede, Phys. Rev. Lett. **76**, 479 (1996).

[59] H. Dai, E. W. Wong, and C. M. Lieber, Science **272**, 523 (1996).

[60] B. L. Altshuler and A. G. Aronov, Solid State Communication **36**, 115 (1979); B. L. Altshuler, A. G. Aronov, and P. A. Lee, Phys. Rev. Lett. **44**, 1288 (1980).

[61] R. Egger and A. O. Gogolin, cond-mat/0101246.

[62] H. Ajiki and T. Ando, J. Phys. Soc. Japan **62**, 1255 (1993).

[63] T. Hertel, R. Martel, and P. Avouris. J. Phys. Chem B **102**, 910 (1998); L. Roschier, J. Penttila, M. Martin, P. Hakonen, M. Paalanen, U. Tapper, E. I. Kauppinen, C. Journet, and P. Bernier, Appl. Phys. Lett. **75**, 728 (1999).

[64] Y. Imry and Z. Ovadyahu, Phys. Rev. Lett. **49**, 841 (1982).

[65] M. H. Devoret, D. Esteve, H. Grabert, G.-L. Ingold, H. Pothier, and C. Urbina, Phys. Rev. Lett. **64**, 1824 (1990); S. M. Grivin, L. I. Glazman, M. Johnson, D. R. Penn, and M. D. Stiles, Phys. Rev. Lett. **64**, 3183 (1990).

[66] K. A. Matveev and L. I. Glazman, Phys. Rev. Lett. **70**, 990 (1993).

[67] R. Egger, Phys. Rev. Lett. 83, 5547 (1999).

[68] A. Kamenev and A. Andreev, Phys. Rev. B **60**, 2218 (1999).

[69] J. Rollbühler and H. Grabert, cond-mat/0102010.

[70] E. Scheer, W. Belzig, Y. Naveh, M.H. Devoret, D. Esteve, and C. Urbina, Phys. Rev. Lett. **86**, 284 (2001).

[71] A.F. Mopurgo, J. Kong, C.M. Marcus, and H. Dai, Science **286**, 263 (1999).

[72] D.L. Cox and M.B. Maple, Phys. Today **48**, No. 2, 32-40 (1995).

[73] D. Goldhaber-Gordon, H. Shtrikman, D. Mahalu, D. Abusch-Magder, U. Meirav, and M.A. Kastner, Nature (London) **391**, 156 (1998).

[74] S.M. Cronenwett, T.H. Oosterkamp, and L.P. Kouwenhoven, Science **281**, 540 (1998).

[75] M.R. Buitelaar, A. Bachtold, T. Nussbaumer, M. Iqbal, and C. Schönenberger, Phys. Rev. Lett. **88**, 156801 (2002).

[76] Y. Meir, N.S. Wingreen, and P.A. Lee, Phys. Rev. Lett. **70**, 2601 (1993).

[77] D. Goldhaber-Gordon, J. Göres, M.A. Kastner, H. Shtrikman, D. Mahalu, and U. Meirav, Phys. Rev. Lett. **81**, 5225 (1998).

[78] D.C. Ralph, C.T. Black, and M. Tinkham, Phys. Rev. Lett. **74**, 3241 (1995).

[79] A. Levy Yeyati, J.C. Cuevas, A. López-Dávalos, and A. Martín-Rodero, Phys. Rev. B **55**, R6137 (1997).

[80] G. Johansson, E.N. Bratus, V.S. Shumeiko, and G. Wendin, Phys. Rev. B **60**, 1382 (1999).

[81] A.A. Abrikosov and L.P. Gor'kov, Sov. Phys. JETP **12**, 1243 (1961).

[82] L.I. Glazman and K.A. Matveev, JETP Lett. **49**, 659 (1989).

[83] Y. Avishai, A. Golub, and A.D. Zaikin, Phys. Rev. B **67**, 041301 (2003).

[84] A.Yu. Kasumov, R. Deblock, M. Kociak, B. Reulet, H. Bouchiat, I.I. Khodos, Yu.B. Gorbatov, V.T. Volkov, C. Journet, and M. Burghard, Science **284**, 1508 (1999).

[85] A. Steinbach, P. Joyez, A. Cottet, D. Esteve, M.H. Devoret, M.E. Huber, and J.M. Martinis, Phys. Rev. Lett. **87**, 137003 (2001).

[86] P. Recher, E.V. Sukhorukov, and D. Loss, Phys. Rev. B **63**, 165314 (2001).

[87] C. Bena, S. Vishveshwara, L. Balents, and M.P.A. Fisher, Phys. Rev. Lett. **89**, 037901 (2002).

[88] Y. Avishai, A. Golub, and A.D. Zaikin, Phys. Rev. B **63**, 134515 (2001).

[89] M. R. Buitelaar, A. Bachtold, T. Nussbaumer, M. Iqbal, and C. Schönenberger, Phys. Rev. Lett. **88**, 156801 (2002).

[90] M. R. Buitelaar, T. Nussbaumer, and C. Schönenberger, Phys. Rev. Lett. **89**, 256801 (2002).

[91] J. Rammer and H. Smith, Rev. Mod. Phys. **58**, 323 (1986).

[92] G. Johansson, V.S. Shumeiko, E.N Bratus, and G. Wendin, Physica C **293**, 77 (1997).

[93] A.B. Zorin, Rev. Sci. Instrum. **66**, 4296 (1997).

[94] J. Nygård and D.H. Cobden, Appl. Phys. Lett. **79**, 4216 (2001).

[95] A. Bezryadin, C.N. Lau, and M. Tinkham, Nature **404**, 971 (2000).

[96] A.N. Cleland and M.L. Roukes, Appl. Phys. Lett. **69**, 2653 (1996).

[97] P.G. Collins, M. Hersam, M. Arnold, R. Martel, and Ph. Avouris, Phys. Rev. Lett. **86**, 3128 (2001).

[98] Z. Yao, C.L. Kane, and C. Dekker, Phys. Rev. Lett. **84**, 2941 (2000).

Publication list

Publications in journals and proceedings:

- *Multiple Andreev Reflections in a Carbon Nanotube Quantum Dot*, M.R. Buitelaar, W. Belzig, T. Nussbaumer, B. Babić, C. Bruder, and C. Schönenberger, Phys. Rev. Lett. **91**, 057005 (2003).
- *Quantum Dot in the Kondo Regime Coupled to Superconductors*, M.R. Buitelaar, T. Nussbaumer, and C. Schönenberger, Phys. Rev. Lett. **89**, 256801 (2002).
- *Multiwall Carbon Nanotubes as Quantum Dots*, M.R. Buitelaar, A. Bachtold, T. Nussbaumer, M. Iqbal, and C.Schönenberger, Phys. Rev. Lett. **88**, 156801 (2002).
- *Suppression of Tunneling into Multiwall Carbon Nanotubes*, A. Bachtold, M. de Jonge, K. Grove-Rasmussen, P.L. McEuen, M. Buitelaar, and C. Schönenberger, Phys. Rev. Lett. **87**, 166801 (2001).
- *Doping State of Multiwall Carbon Nanotube Wires and Quantum Dots*, C. Schönenberger, M.R. Buitelaar, M. Krüger, I. Widmer, T. Nussbaumer, and M. Iqbal, Proceedings of the 36th Rencontres de Moriond, Les Arcs, France (2001).
- *Electrochemical Carbon Nanotube Field-Effect Transistor*, M. Krüger, M.R. Buitelaar, T. Nussbaumer, L. Forró, and C. Schönenberger, Appl. Phys. Lett. **78**, 1291 (2001).
- *Spatially Resolved Scanning Tunneling Spectroscopy on Single-Walled Carbon Nanotubes*, L.C. Venema, J.W. Janssen, M.R. Buitelaar, J.W.G. Wildöer, S.G. Lemay, L.P. Kouwenhoven, and C. Dekker, Phys. Rev. B **62**, 5238 (2000).

Invited talks:

- *A Carbon Nanotube Quantum Dot in the Kondo Regime Coupled to Superconductors*, Invited talk at the 287. WE-Heraeus-Seminar, Bad Honnef, Germany, October 2002.
- *Multiwall Carbon Nanotube Wires and Quantum Dots*, Seminar talk at the groups of C. Strunk and D. Weiss, Regensburg, Germany, June 2002.
- *Multiwall Carbon Nanotubes as Quantum Wires and Dots*, Seminar talk at the group of R. Egger, Düsseldorf, Germany, December 2001.

Curriculum Vitae

Mark Robertus Buitelaar

26. 4. 1974	Born in Den Haag, the Netherlands.
1986-1992	Atheneum at the Corderius College in Amersfoort.
1992-1998	M.Sc. in Applied Physics at Delft University of Technology. Graduate research in the Quantum Transport group under the supervision of prof. dr. C. Dekker and prof. dr. ir J.E. Mooij. Subject: 'Scanning tunneling microscopy and spectroscopy on single wall carbon nanotubes'.
1999-2002	Ph.D. research at Basel University in the group of prof.dr. C. Schönenberger. Subject: 'Electron transport in multiwall carbon nanotubes'.
2002-	Postdoctoral research associate at Cambridge University.

Acknowledgements

This thesis work could not have been done without the support of a number of people. I would like to thank my Ph.D. advisor Christian Schönenberger who has always been full of enthusiasm and ideas. I have learned a lot from you. While allowing me a lot of freedom, you always found time in a busy schedule to discuss physics or technical issues when needed. I have very much appreciated working together with you.

I would also like to thank Adrian Bachtold who introduced me to the different fabrication facilities and who had already successfully started the work on carbon nanotubes in Basel. I furthermore very much enjoyed the company of the other Ph.D. students in those first years: François Dewarrat, Tilman Hoss, Michael Krüger, Stefan Oberholzer and Christophe Terrier. Later on these were followed by Bong-Ryoul Choi, Bakir Babić, Lucia Grüter, Soufiane Ifadir, Sangeeta Sahoo and Jürg Furer.

Perhaps the most peculiar characters which have been present during my stay in Basel are the postdocs. I would like to acknowledge the support of Michel Calame, Shadyar Farhangfar, Hans-Werner Fink, Adam Hansen, Mahdi Iqbal, Derek Kelly, Zuqin Liu and Christoph Strunk. I would especially like to thank Thomas Nussbaumer who has done a great deal of work on the TLM 400 dilution fridge which has been essential for several of the measurements presented in this thesis. Finally, the stories of Dinko Babić ensured that I knew everything I needed to know about Cambridge long before I eventually went to work there myself.

It has also been a pleasure to be able to collaborate with people from outside the group. I would especially like to mention Christoph Bruder and Wolfgang Belzig of the theory department. It has taken some time and a number of computer crashes but eventually the model calculations of a single resonant level coupled to superconducting leads has helped a lot in our understanding of the experimental data. We were furthermore very fortunate to receive the necessary high quality MWNT powder from the group of László Forró in Lausanne. Also the support from the mechanical and electronic workshops has been indispensable. I would in particular like to thank Herr Roth for the steady supply of nitrogen and liquid helium.

Finally, I would like to thanks all my family and friends who have been there for me during my stay in Basel. I would especially like to thank my partner Liesbeth for her patience, love, and support. With the arrival of our daughter Femke, our new lives in Cambridge could not have started better.